Mesoscale Atmospheric Systems -

Observation and Modelling

Prof. Huw C. Davies

Contents

Textbooks and Source Material

Aktinson, B. W. 1981 , 'Meso-Scale Atmospheric Circulations', Academic Press, London.

Lilly, D. K. and T. Gal-Chen (Eds.), 1983, 'Mesoscale Meteorology - Theories, Observations and Models', D. Reidel, Boston.

Pielke, R. A. 1984,' Mesoscale Meteorological Modeling', Academic Press, London.

Ray, P. S. (Ed.) 1987, 'Mesoscale Meteorology and Forecasting', American Meteorological Society, Boston.

Chapter 1

INTRODUCTION

1.1 Descriptive Definition

Mesometeorology encompasses the study of phenomena that possess characteristic time and/or horizontal space scales that are intermediate between macro- (≥ 2 days, ≥ 2000 km) and micro- (≤ 20 mins, ≤ 2 km) scale systems.

The distribution of an assemblage of atmospheric circulation systems, in terms of their characteristic time (T) and horizontal space scale (L) is shown in Table 1.1 (Caveats: an atmospheric phenomenon often exhibits considerable variability from event to event, systems are often anisotropic in the horizontal, the local and the advective time scales need not be comparable.)

1.2 Range of Mesoscale systems

A wide and disparate range of phenomena fall into the mesoscale category. For instance Mesometeorology embraces the study of:

- internal thermal transition zones with L$\approx$ 2 and 200 km
- destructive wind systems with L$\approx$2, 20 and 200 km.

The understanding, prediction (and perhaps the modification) of the rich diversity of systems on this scale constitutes the distinctive challenge of Mesometeorology.

In view of this large range of phenomena a further subdivision might prove helpful. One suggested scheme (- defined in terms of the characteristic horizontal length scale) is indicated in Table 1.1.

A list of some distinctive mesoscale phenomena is appended here:

Meso-α: Surface and upper-level fronts; jet stream features; frontal wave families; hurricanes;

Meso-β: Squall lines and severe storms; sea, lake and land breezes; heat islands; mountain wave disturbances; Fohn; low-level nocturnal jets; cloud clusters;

Meso-γ: Lee waves; clear-air turbulence and billows; cloud bands and arcs; slope winds.

Table 1.1: Einteilung atmosphärischer Phänomene nach ihren charakteristischen Längenabmessungen und ihrer Zeitdauer (nach Orlanski, 1975)

T_s / L_s	1 MONAT	1 TAG	1 STUNDE	1 MINUTE	1 SEKUNDE
10 000 km	Allgemeine Zirkulation, Lange Wellen				MAKRO-SKALA α
2 000 km		Barokline Wellen			MAKRO-SKALA β
200 km		Fronten, Tropische Zyklonen			MESO-SKALA α
20 km			Orographische Effekte, LandSee-Wind, Wolkenhaufen		MESO-SKALA β
2 km			Gewitter, Interne Schwere Wellen, Urbane Wärmeinsel		MESO-SKALA γ
200 km				Tornados, Konvektion	MIKRO-SKALA α
20 m				Staubtromben, Thermik	MIKRO-SKALA β
m				Kleinräumige Turbulenz	MIKRO-SKALA γ
	MAKROSKALA	MESOSKALA	MIKROSKALA		

1.3 Remarks on the Nature of Mesoscale Systems

- Several physical processes can play a significant role within a single mesoscale system e.g. during the development of a sea-breeze circulation the following processes can act sequentially: radiation, conduction, dry convection / turbulent transport, thermally induced horizontal pressure gradients, pressure gradient induced winds, thermal overturning and moist convection, Coriolis induced wind turning.

- The relative importance of individual processes can differ substantially from one kind of system to another (e.g. condensational effects) and even from one-event-to-another of the same system.

- Mesoscale systems can be both embedded within a macroscale system and contain within their circulation pattern one, or several types of, smaller scale phenomena. An important repercussion is that mesoscale systems can be influenced by, and interact with, both larger and smaller scale flow systems.

Thus mesoscale phenomena can exhibit an interplay of several physical processes, an interdependence and co-existence of various scales.

1.4 On the Origin of Mesoscale Systems

- Terrain variations (e.g. orography, surface characteristics) possessing mesoscale spatial dimensions can provide a direct forcing of the atmosphere on this scale. (External mesoscale forcing.)

- Synoptic scale flow features could develop a mesoscale structure (internal macro-scale forcing).

- Synoptic scale could provide suitable setting for the development of free mesoscale flow systems (Mesoscale instabilities).

- Interaction of two mesoscale systems could generate a third mesoscale system (internal mesoscale forcing).

- Ensemble effect of smaller scale systems could interact synergetically to yield a mesoscale system (internal micro-scale forcing).

One approach to mesoscale studies (- and the one followed here) is to establish a classification of mesoscale phenomena based on the above categories. (Caveat: certain phenomena might be the result of the interaction of phenomena from different categories.)

1.5 The Observation of Mesoscale Systems

An adequate description of a mesoscale circulation requires (by definition) a knowledge of the atmosphere on a space scale that is less than that definable with the standard radiosonde network and greater than that sampled with the customary range of in-situ sensors at a single station. It is worth noting that most of the 'significant' weather occurs in conjunction with mesoscale systems and can often remain undetected within the conventional synoptic-scale network ($L \geq 400\,\text{km}$, $T \approx 12$ hrs).

In recent years a state of new mesoscale-related observational tools have become available for research and/or operational use, and numerous other techniques are in the development phase. For example many weather services now have available to them on a quasi-continuous, real-time basis:

- mesoscale (space and time) networks of automatic surface sampling stations,
- mesoscale digitalised displays from arrays of conventional radar,
- fine resolution 'visible' and 'IR' satellite imagery.

Recent development in Doppler radar technology (clear air, polarization diversity, etc), Lidar (incoherent and coherent pulsed systems), refined satellite based temperature and humidity profiling, and ground based quasi-continuous wind profiling all represent future potentially operational systems. In addition research aircraft flights, instrumented masts and tethered balloons are other important research tools.

Research studies of particular phenomena require as a central component the undertaking of a field experiment. The design of a comprehensive and systematic observational programme poses a formidable scientific, logistic, instrumental and economic challenge. Thus considerable forethought must be exercised in establishing the precise scientific objectives, in specifying the observational requirements, and in the choice and deployment of observational tools.

Chapter 2

BASIC THEORETICAL CONSIDERATIONS

2.1 Scale Analysis

Here we follow the procedure outlined earlier (Atmosphärenphysik II) and undertake a scale analysis of the basic governing equations for certain individual phenomena. This exercise serves two related purposes. It yields estimates of the order of magnitude of the various terms in each of the equations and concomitantly provides some justification for discarding terms whose relative magnitude is small.

In Table 2.1 characteristic values have been assigned for the field variables for a range of circulation systems (viz. baroclinic waves, fronts, low-level jets, clear-air-turbulence and isolated convective plume, - corresponding respectively to macro-β, meso-α, β, γ and micro-α scales). Caveat: the values at a given scale do not necessarily typify all phenomena at that scale.

The results of the procedure are shown in Table 2.2i-v). It appears reasonable to conclude that for the mesoscale systems considered:

- earth's sphericity and the β-effect are not significant,
- Coriolis effect is such that $Ro \sim 1$, (> 1, $\gg 1$) for respectively meso-α (-β, -γ) systems,
- mesoscale density and potential temperature fluctuations are directly related ($\rho^*/\rho_0 \approx \Theta^*/\Theta_0$),
- compressibility effects are secondary and enter only via the mean state density variation,
- non-hydrostatic effects become significant on the meso-γ scale.

Note that the scale analysis procedure emphasizes the intermediate nature of the mesoscale from another standpoint - within the mesoscale several dimensionless parameters (e.g. Ro, D/H, UT/L) traverse near the value of unity.

2.2 The Anelastic System

It also follows from the result displayed in Table 2.2 that the dynamics of the entire mesoscale should be reasonably represented by the following set of equations - the Anelastic Equations -,

$$\begin{aligned}
\frac{Du}{Dt} - fv &= -\frac{\partial}{\partial x}\left(\frac{p^*}{\rho_0}\right) \\
\frac{Dv}{Dt} + fu &= -\frac{\partial}{\partial y}\left(\frac{p^*}{\rho_0}\right) \\
\delta\frac{Dw}{Dt} &= -\frac{\partial}{\partial z}\left(\frac{p^*}{\rho_0}\right) + g\frac{\Theta^*}{\Theta_0} \\
\frac{\partial u}{\partial x} + \frac{\partial v}{\partial y} + \left(\frac{\partial}{\partial z} - \frac{1}{\kappa}\right)w &= 0 \\
\frac{1}{\Theta_0}\cdot\frac{D\Theta^*}{Dt} &= \frac{1}{c_pT}Q \\
\frac{\rho^*}{\rho_0} &= -\frac{\Theta^*}{\Theta_0}
\end{aligned} \tag{2.1}$$

where:

$$\frac{D}{Dt} = \left\{\frac{\partial}{\partial t} + u\frac{\partial}{\partial x} + v\frac{\partial}{\partial y} + w\frac{\partial}{\partial z}\right\} \tag{2.2}$$

with:

$$\kappa^{-1} = \frac{1}{\rho_0}\cdot\frac{\partial\rho_0}{\partial z} \tag{2.3}$$

and δ is a dummy variable such that $\delta = (0, 1)$ refers respectively to hydrostatic and non-hydrostatic flow systems and Q refers to the diabatic heating. This set has a much simpler form than the original full set - it represents the flow of an inviscid, almost-incompressible fluid on an f-plane. For individual phenomena it is clear that it can be simplified further.

The reduced system satisfies an appropriate energy relationship. With $Q \equiv 0$ and with the isentropic base state ($\Theta_0 \equiv$ constant), then it can be shown that within a closed (or periodic) domain V:

$$\frac{\partial}{\partial t}\int\int\int_V \left\{\frac{1}{2}\rho_0(u^2 + v^2 + \delta w^2) - \left(\rho_0\frac{g}{\Theta_0}\right)\Theta^*\cdot z\right\} dV \equiv 0 \tag{2.4}$$

i.e. system satisfies an energy conservation principle, and the energy integral comprises the sum of a kinetic energy, $1/2\rho_0(u^2 + v^2 + \delta w^2)$, and a pseudo-potential energy, $(\rho_0 \cdot g/\Theta_0)\Theta^* \cdot z$. There is no explicit reference to internal or elastic energy in the integral invariant and hence the name - anelastic equations.

Note that the ratio of the two terms yield another dimensionless parameter - the Froude Number (F) or its inverse $\mathscr{F}$, where,

$$F = U/NH, \text{ or } \mathscr{F} = F^{-1} = NH/U \tag{2.5}$$

(here we have chosen the representation $g/\Theta_0 \cdot \Theta^* z \approx N^2H^2$.) Hence this number relates to the ratio of the kinetic energy to the work required (or the potential energy change) in raising a fluid element a distance H in an uniformly stratified atmosphere.

Table 2.1: Some order of magnitude estimates of the characteristic values of atmospheric variables.

Scale of System	Time	Length Scales		Velocity Fields		Thermodynamic Fields	
		Horizontal	Vertical	Horizontal	Vertical	Scaled pressure	Pot. Temp.
	$[T]$ s	$[L]$ m	$[D]$ m	$[U, \Delta U]$ m/s	$[W, \Delta W]$ m/s	$[\Delta p^*/\rho_0]$ m^2/s^2	$[\Delta\Theta^*]$ K
Macro-β	10^5	10^6	10^4	10	$\leq 10^{-2}$	10^3	4
Meso-α	10^5	10^5	$5 \cdot 10^3$	10	$\leq 5 \cdot 10^{-2}$	$2 \cdot 10^2$	2
Meso-β	10^4	$5 \cdot 10^4$	$3 \cdot 10^3$	10	$\leq 10^{-1}$	$2 \cdot 10^2$	2
Meso-γ	10^3	$5 \cdot 10^3$	10^3	10	1	10^2	2
Micro-α	$5 \cdot 10^2$	10^3	$5 \cdot 10^3$	1	3	10	10^{-1}

Table 2.2: Scale Analysis of the Basic Equations

i) Eastwards horizontal momentum equation:

	Du/Dt $[U/T, U^2/L, UW/D]_{max}$	$f_0 \cdot v$ $[f_o U]$	$(\beta y) \cdot v$ $[4\beta LU]$	$e \cdot w$ $[eW]$	$u \cdot w/a$ $[UW/a]$	$uv \cdot \tan\phi/a$ $[U^2/a]$	$1/\rho \cdot \partial p/\partial x$ $[\Delta p^*/\rho_0 L]$
Macro-β	10^{-4}	10^{-3}	10^{-4}	10^{-6}	10^{-8}	10^{-5}	10^{-3}
Meso-α	10^{-3}	10^{-3}	10^{-4}	$5 \cdot 10^{-6}$	10^{-7}	10^{-5}	10^{-3}
Meso-β	$5 \cdot 10^{-3}$	10^{-3}		10^{-5}	10^{-7}	10^{-5}	$4 \cdot 10^{-3}$
Meso-γ	10^{-2}	10^{-3}		$5 \cdot 10^{-4}$	10^{-6}	10^{-5}	10^{-2}
Micro-α	10^{-2}	10^{-4}		10^{-4}	10^{-6}	10^{-7}	10^{-2}

ii) Modified gas equation:

	ρ^*/ρ_0	$1/c^2 \cdot p^*/\rho_0$	Θ^*/Θ_0
Macro-β	-	10^{-2}	10^{-2}
Meso-α	-	10^{-3}	10^{-2}
Meso-β	-	10^{-3}	10^{-2}
Meso-γ	-	10^{-3}	10^{-2}
Micro-α	-	10^{-4}	10^{-3}

iii) Thermodynamic equation:

	$1/\Theta_0 \cdot D_h\Theta^*/Dt$	$w \cdot 1/\Theta_0 \cdot \partial\Theta_0/\partial z$	$w \cdot 1/\Theta_0 \cdot \partial\Theta^*/\partial z$	q/c_pT_0
Macro-β	10^{-7}	$w \cdot 10^{-5}$	$w \cdot 10^{-6}$	$4(n) \cdot 10^{-8}$
Meso-α	10^{-6}	$w \cdot 10^{-5}$	$w \cdot 10^{-6}$	
Meso-β	10^{-6}	$w \cdot 10^{-5}$	$w \cdot 10^{-6}$	
Meso-γ	10^{-5}	$w \cdot 10^{-5}$	$w \cdot 10^{-5}$	
Micro-α	10^{-5}	$w \cdot 10^{-5}$	$w \cdot 10^{-5}$	

iv) Mass conservation equation:

	$1/\rho_0 \cdot D_h\rho^*/Dt$ $[\Delta\rho^*/\rho_0 T, \Delta\rho^*/\rho_0 \cdot U/L]_{max}$	$w \cdot S$ $[W \cdot S]$	$\partial w/\partial z$ $[W/D]$	$\nabla_h \cdot v_h$ $\leq [U/L]$
Macro-β	10^{-7}	10^{-6}	10^{-6}	
Meso-α	10^{-6}	$5 \cdot 10^{-6}$	10^{-5}	
Meso-β	10^{-6}	10^{-5}	10^{-5}	
Meso-γ	$3 \cdot 10^{-5}$	10^{-4}	10^{-3}	
Micro-α	10^{-6}	10^{-4}	10^{-3}	

v) Vertical momentum equation:

	Dw/Dt $[W/T, UW/L, W^2/D]_{\max}$	$e \cdot u$ $[e \cdot U]$	$(u^2+v^2)/a$ $[U^2/a]$	$(\partial/\partial z - N^2/g) \cdot p^*/\rho_0$ $[\Delta p^*/\rho_0 D]$	$[\Delta p^*/\rho_0 \cdot N^2/g]$	$g \cdot \Theta^*/\Theta_0$ $[g \cdot \Delta\Theta^*/\Theta_0]$
Macro-β	10^{-7}	10^{-3}	10^{-5}	10^{-1}	10^{-2}	10^{-1}
Meso-α	10^{-6}	10^{-3}	10^{-5}	$4 \cdot 10^{-2}$	10^{-3}	$4 \cdot 10^{-2}$
Meso-β	10^{-5}	10^{-3}	10^{-5}	$6 \cdot 10^{-2}$	10^{-3}	$6 \cdot 10^{-2}$
Meso-γ	10^{-2}	10^{-3}	10^{-5}	$3 \cdot 10^{-2}$	10^{-3}	$4 \cdot 10^{-2}$
Micro-α	10^{-3}	10^{-4}	10^{-7}	$2 \cdot 10^{-3}$	10^{-3}	10^{-3}

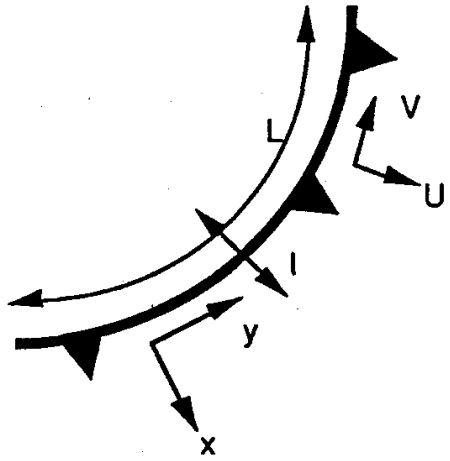

Figure 2.1: Along and Across front coordinate system

2.3 The Semi-Geostrophic System

The set of equations represented by the anelastic system is appropriate for most mesoscale circulation systems. There is an even simpler set that is intermediate between the anelastic set and the conventional quasi-geostrophic system.

A rationale for this set can be illustrated as follows:

Consider a flow pattern that is horizontally anisotropic (e. g. a front, see Fig. 2.1), and has characteristic spatial and velocity scales such that $(U/V) \ll 1$, $(1/L) \ll 1$, with $(U/V)(1/L)^{-1} \approx 1$.

Then scaling arguments can be introduced to indicate that

$$\left\| \left(\frac{Du}{Dt} \right) / fv \right\| \approx (U/fL) = R_{\text{across}} \tag{2.6}$$

$$\left\| \left(\frac{Dv}{Dt} \right) / fu \right\| \approx (V/fl) = R_{\text{along}} \tag{2.7}$$

where R_{across} and R_{along} denote respectively across and along front Rossby Numbers. If, for a given flow system, $R_{\text{across}} \ll R_{\text{along}} \leq 1$, then it would be appropriate to neglect the Du/Dt term in Equations (2.1) and assume geostrophy for the velocity component in the elongated direction, i.e. assume the system is semi-geostrophic.

A further extension of this procedure is the geostrophic momentum approximation. In this limit the advective operator, D/Dt, in the set of Equations (2.1) is replaced as follows,

$$\frac{D}{Dt}(u, v, w, \Theta^*) \Rightarrow \left\{ \frac{\partial}{\partial t} + (u_G + u_a)\frac{\partial}{\partial x} + (v_G + v_a)\frac{\partial}{\partial y} \right\}(u, v, w, \Theta^*) \tag{2.8}$$

where on the right hand side $(u, v) = (u_G + u_a, v_G + v_a)$ and (u_G, v_G) and (u_a, v_a) refer respectively to the geostrophic and ageostrophic velocities. Both the semi-geostrophic and the

geostrophic momentum sets possess appropriate integral relationships.

2.4 Free Oscillations of the Anelastic System

An examination of the small amplitude free oscillations that the Anelastic System can sustain will yield

- the detailed wave properties of the linearized system,
- insight on the nature of the system (incl. it likely response to external forcing),
- starting point for the understanding of the more complex and/or non-linear flow configurations.

Now we apply the standard perturbation technique. In addition to the $\chi = \{\chi_0(z) + \chi^*\}$ decomposition of the field variables (where the zero subscript refers to an isentropic state of the motion), the χ^* field is further separated into unperturbed and perturbed components, i. e. $\chi^* = \bar{\chi} + \chi'$, with $||\chi'|| \ll \bar{\chi}$.

The unperturbed state is taken to be an uniformly stratified atmosphere ($N^2 = g/\Theta_0 \cdot d\bar{\Theta}/dz = \text{const}$) in uniform motion, U, i. e.

$$\overrightarrow{v^*} = (U, 0, 0) + (u', v', w') \tag{2.9}$$

$$(\Theta^*, p^*) = [\bar{\theta}(z), \bar{p}(z) + (\Theta', p')], \tag{2.10}$$

with

$$fU = -\frac{\partial}{\partial y}\left(\frac{\bar{p}}{\rho_0}\right) \tag{2.11}$$

The linearized equations for the perturbation variables take the form,

$$\mathscr{L}u' - fv' = -\left(\frac{p'}{\rho_0}\right)_x \tag{2.12}$$

$$\mathscr{L}v' + fu' = -\left(\frac{p'}{\rho_0}\right)_y \tag{2.13}$$

$$\mathscr{L}w' = -\left(\frac{p'}{\rho_0}\right)_z + b' \tag{2.14}$$

$$u'_x + v'_y + w'_z - \frac{1}{H}w' = 0 \tag{2.15}$$

$$\mathscr{L}b' + N^2 w' = 0 \tag{2.16}$$

where $\mathscr{L}$ refers to the advective operator ($\mathscr{L} = \partial/\partial t + U\partial/\partial x$), H to the scale height, ($H = 1/\rho_0 \cdot \partial\rho_0/\partial z$) and the expression for the buoyancy, b' is given by: $b' = g\frac{\Theta'}{\Theta_0}$.

The above set can be reduced to a single equation for the perturbation vertical velocity (w'):

First derive expressions for the time rate of change of the horizontal divergence ($D' = u'_x + v'_y$) and the vertical component of the vorticity, ($\zeta = v'_x - u'_y$). These take the form,

$$\mathscr{L}D' - f\zeta' = -\nabla_h^2\left(\frac{p'}{\rho_0}\right), \tag{2.17}$$

$$\text{and} \quad \mathscr{L}\zeta' - fD' = 0. \tag{2.18}$$

Eliminating between these two equations yields

$$\left(\mathscr{L}^2 + f^2\right) D' = -\nabla_h^2 \mathscr{L}\left(\frac{p'}{\rho_0}\right) \tag{2.19}$$

Using sequentially the continuity and vertical momentum equations gives

$$\left(\mathscr{L}^2 + f^2\right)\left(\frac{\partial}{\partial z} - \frac{1}{H}\right) w' = \nabla_h^2 \mathscr{L}\left(\frac{p'}{\rho_0}\right) \tag{2.20}$$

$$\frac{\partial}{\partial z}\left(\mathscr{L}^2 + f^2\right)\left(\frac{\partial}{\partial z} - \frac{1}{H}\right) w' = \mathscr{L}\nabla_h^2\left[-\delta\mathscr{L}^2 w' + b'\right] \tag{2.21}$$

$$= -\left[\delta\mathscr{L}^2 + N^2\right]\nabla_h^2 w' \tag{2.22}$$

$$\boxed{\left(\mathscr{L}^2 + f^2\right)\frac{\partial}{\partial z}\left(\frac{\partial}{\partial z} - \frac{1}{H}\right) w' + \left(\delta\mathscr{L}^2 + N^2\right)\nabla_h^2 w' = 0} \tag{2.23}$$

This is a partial differential equation with constant coefficients (f, H and N^2 are constant), and it is appropriate to seek solutions of the form

$$w' = W(z)\mathrm{e}^{\mathrm{i}(kx+ly-wt)} \tag{2.24}$$

This leads to the relationship

$$W_{zz} - \frac{1}{H}W_z + n^2 W = 0, \tag{2.25}$$

$$\text{where } n^2 = \frac{(N^2 - \delta\tilde{\omega}^2)}{(\tilde{\omega}^2 - f^2)}K^2, \tag{2.26}$$

$$\text{with } \tilde{\omega} = (\omega - kU) \text{ and } K^2 = k^2 + l^2 \tag{2.27}$$

On introducing the variable $\chi(z) = W\mathrm{e}^{-z/2H}$, this equation transforms into the compact form,

$$\boxed{\chi_{zz} + \left(n^2 - \frac{1}{4H^2}\right)\chi = 0} \tag{2.28}$$

It follows that the vertical structure of the perturbations depend crucially upon the value of the parameter $\lambda^2 = n^2 - 1/(4H^2)$.

The structure is - exponential for $\lambda^2 < 0$,
- oscillatory for $\lambda^2 > 0$.

In the former case the perturbations can satisfy a 'zero' - boundary condition at only one level, and are therefore termed external waves. In the latter case such a condition can be satisfied at two levels and the waves are termed internal.

A dispersion diagram showing the internal and external wave regimes in the parameter space of $(\tilde{K}, \tilde{\omega})$ is shown in Fig. 2.3. Cross reference with Table 1.1 indicates that there is a qualitative correspondence between the region of parameter space occupied by observed mesoscale phenomena and the region occupied by waves for which $\|\tilde{\lambda}^2\| \approx (2\pi)^2 - (20\pi)^2$ i. e. waves with a vertical wavelength (or e^{-1} folding distance) that is of the order of, or a significant fraction of the tropospheric depth.

The dispersion relationship,

$$\tilde{\omega}^2 = \frac{N^2K^2 + n^2f^2}{\delta K^2 + n^2} \tag{2.29}$$

indicates that:

- the waves owe their existence to the earths rotation (f) and the vertical stratification (N). Hence the term "inertia-buoyancy waves",
- the omission of the β-effect excludes the occurrence of Rossby waves, and the anelastic form of the mass conservation relationship also excludes acoustic waves,
- internal waves (- and hence vertical propagation effects) can occur in a wedge-shaped region of the $(\tilde{K}, \tilde{\omega})$ domain within the frequency band $f \to\sim N$ (see Fig. 2.2).

Note the following three limit forms of the dispersion relationship:

- hydrostatic, rotating system,	$\tilde{\omega}^2 = N^2(K/n)^2 + f^2$	(a)
- hydrostatic, non-rotating system,	$\tilde{\omega}^2 = N^2(K/n)^2$	(b)
- nonhydrostatic, non-rotating system,	$\tilde{\omega}^2 = N^2K^2/(K^2 + n^2)$	(c)

These three forms provide, between them, a good approximation to the full relationship across the entire internal-wave domain.

Another illuminating viewpoint from which to examine the dispersion relationship is to set $\tilde{\omega}^2 = U^2k^2$ (i. e. to consider steady state systems). In this case we can determine $n^2 = n^2(k, l)$ for given values of the parameters N, f, U. The result is shown in Fig. 2.2. An internal wave regime exists within the wavenumber band $\{S \to Ro\}$, where $S = Uk/N$ and $Ro = Uk/f$.

Finally we recall that the concept of "Group velocity" can also be utilized to interpret the wave-response of the atmosphere to a localized forcing. In this context note that the perturbation vertical velocity of an internal wave is given by,

$$w' = \chi(z)e^{z/2H}e^{i(kx+ly-wt)} = \mathscr{A}\, e^{i\phi} \tag{2.30}$$

so that $(\mathscr{A}, \phi)$ = Amplitude, phase. Furthermore, if $\tilde{\lambda}^2 \gg 1/4$ i.e. vertical wavelength $\Lambda_D \ll 80\,\text{km}$), then $\lambda \sim n$. In this limit compressibility effects do not influence the vertical wavelength. Hence in this simplified, but realistic, situation the phase and group velocities are given by

$$(u_p, v_p, w_p) = \left(\frac{\omega}{k}, \frac{\omega}{l}, \frac{\omega}{n}\right), \tag{2.31}$$

$$(u_g, v_g, w_g) = \left(\frac{\partial\omega}{\partial k}, \frac{\partial\omega}{\partial l}, \frac{\partial\omega}{\partial n}\right). \tag{2.32}$$

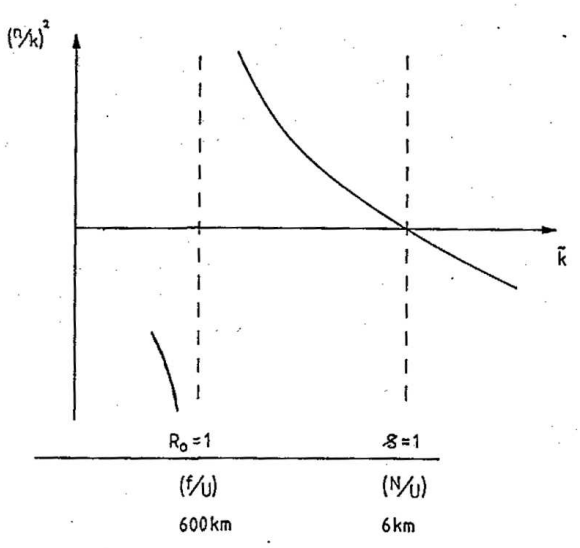

Figure 2.2: Vertical wave-structure as a function of horizontal wavenumber

Depiction of vertical wave-structure as a function of horizontal wavenumber. Let (n, k, l) refer to the vertical and horizontal wavenumbers, and $K = (k^2 + l^2)^{1/2}$.

Relationship for the vertical wave-structure,

$$n^2 = \frac{N^2 - \delta\tilde{\omega}^2}{\tilde{\omega}^2 - f^2}K^2 \quad \Rightarrow \quad n^2 = \frac{N^2 - U^2k^2}{U^2k^2 - f^2}K^2, \text{ for } w = 0 \tag{2.33}$$

Hence

$$\left(\frac{n^2}{K^2}\right) = \left(\frac{N^2}{f^2}\right)\frac{1 - S^2}{Ro^2 - 1} \quad \text{, with } S = Uk/N,\ Ro = Uk/f \tag{2.34}$$

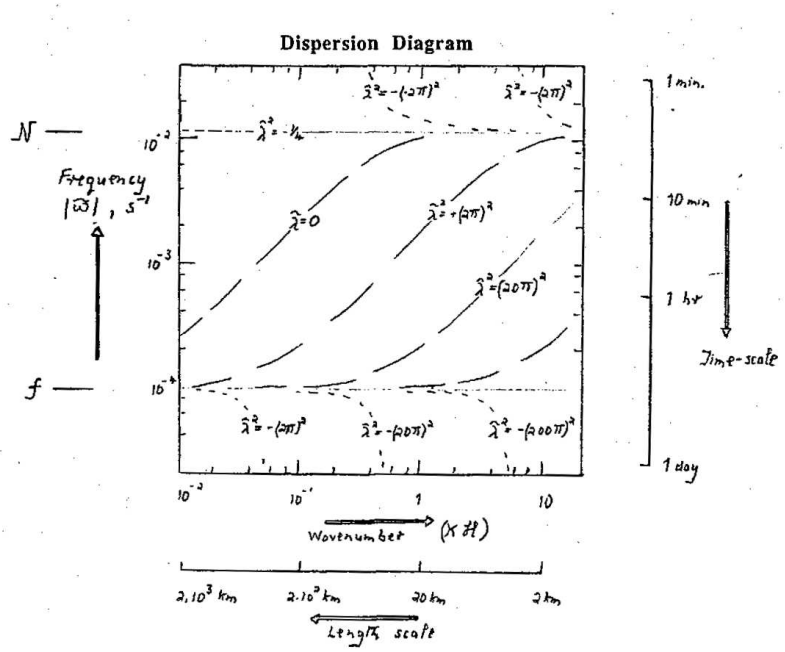

Figure 2.3: Dispersion diagram for the mesoscale.

Dispersion Relationship:

$$\tilde{\omega}^2 = \frac{N^2\tilde{K}^2 + \tilde{n}^2 f^2}{\left[\delta\tilde{K}^2 + \tilde{n}^2\right]} \tag{2.35}$$

with:

$$\tilde{\lambda}^2 = (\tilde{n}^2 - 1/4),\ (\tilde{\lambda}, \tilde{n}, \tilde{K}) = (\lambda, n, K)\mathscr{H}, \tag{2.36}$$

Values used in computation:

$$N^2 = 1.44 \cdot 10^{-4}\, s^{-1}, f = 10^{-4}\, s{-}1, \mathscr{H} = 10^4 m \tag{2.37}$$

and the vertical wavelength, Λ_D, such that $\Lambda_D = 2\pi/\lambda$.

Thus:

Table 2.3: Numerical values for wavelengths vs. wavenumbers.

$\tilde{\lambda}$	$0.2 \cdot \pi$	$2 \cdot \pi$	$20 \cdot \pi$	$200 \cdot \pi$
Λ_D[km]	100	10	1	0.1

Part II: TERRAIN INDUCED SYSTEMS

A schematic sub-division of terrain induced mesoscale systems is shown in Fig 2.4.

In this scheme mesoscale terrain phenomena are split into those that are evident during quiescent or quasi-steady synoptic settings and those present during periods of active synoptic scale activity.

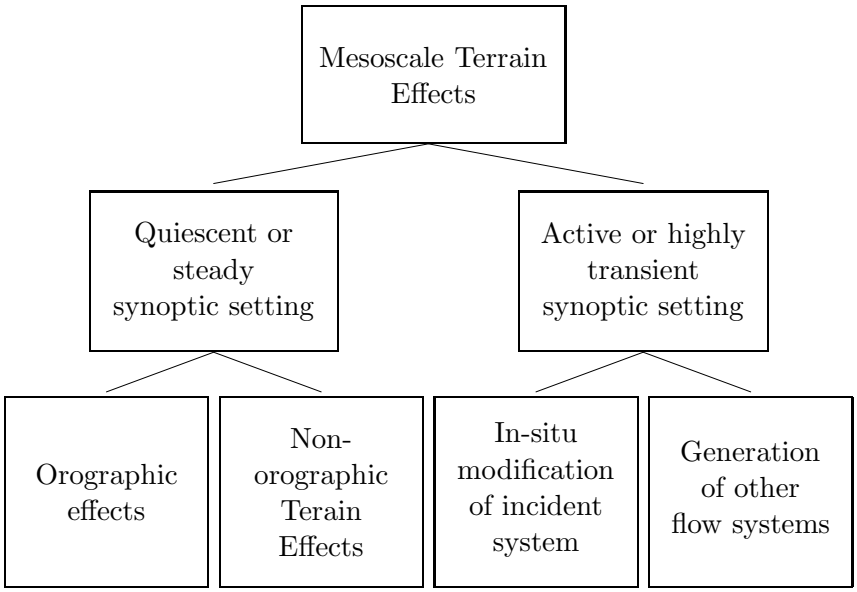

Figure 2.4: Mesoscale terrain phenomena split if occurring during steady or transient synoptic activity.

From a didactic standpoint it is appropriate to first consider the former category. The study of such systems forms the subject matter of PART II, and a discussion of some phenomena that fall into the latter category is presented in a later Chapter.

Chapter 3

OROGRAPHICALLY INDUCED SYSTEMS - MECHANICAL EFFECTS

Phenomena that are classifiable as orographically induced systems are attributable to two distinct (but not necessarily separable) forms of external mesoscale forcing - a mechanical effect induced as an airflow impinges upon an orographic feature, and a thermal effect arising from the differential heating of the atmosphere in the horizontal due to variations in the height of the terrain. In this chapter we consider the first effect in isolation.

3.1 The Parametric Setting

The mechanical effect of mesoscale orographic feature(s) is responsible for a wide variety of flow patterns. The nature of the flow response is related to the structure and strength of the incident airstream and the structure and height of the orography. Consider an uni-directional upstream flow with $\mathbf{v} = (U(z), 0, 0)$, a stratification characterised by $N^2 = N^2(z)$, and an isolated orographic feature with characteristic half-width (L, M) and height η.

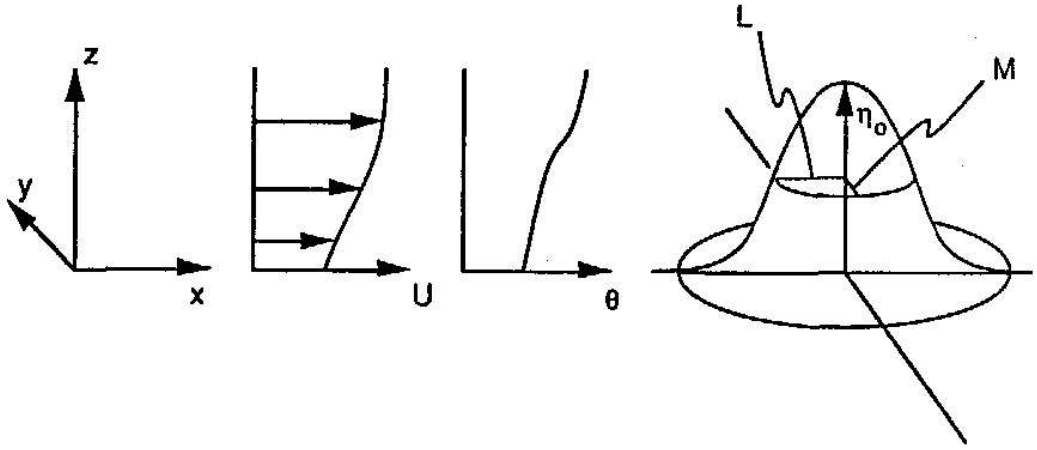

Figure 3.1: Wind and Potential Temperature profiles prior of impinging on a elliptical mountain, with semi-major axis M, semi-minor axis L and of height η_0.

Some key dimensionless numbers for this problem are:

$Ro = \left(\frac{\tilde{U}}{fL}\right)$	- Rossby Number based upon mountain half-width,
$\mathscr{F} = \left(\frac{\tilde{N}\eta_0}{\tilde{U}}\right)$	- inverse Froude Number based upon mountain height,
$\mathscr{S} = \left(\frac{\tilde{N}L}{\tilde{U}}\right)$	- Scorer Parameter (c.f. also Appendix I),
$A_n = L/M$	- horizontal anisotropy of mountain,
$A_s = \eta_0/\tilde{U}$	- aspect ratio of mountain.

Note that not all these numbers are independent and also that $\tilde{U}$ and $\tilde{N}$ are characteristic values for U and N.

Moreover if the incident flow is highly structured in the vertical then other parameters can be significant. For example consider the situation of a strong inversion of strength ($\Delta\Theta$) in the upstream flow at a height H. In this case some additional ratios would be:

	$F = \left(U/(g^* \cdot H)^{1/2}\right)$	- Froude Number based upon inversion height,
	$A_i = (\eta_0/H)$	- scaled inversion height,
Here	$g^* = (g\Delta\Theta/\Theta)$,	- the so-called reduced gravity.

The variety of mesoscale orographic configurations is vast. One dynamical measure of the range of orographic features is illustrated in Fig 3.17. Here various hills and mountains are located in the parameter space of (Ro, $\mathscr{F}$, A_n) under the assumption that $U = 10\,ms^{-1}$, $f_0 = 10^{-4}\,s{-}1$, and $N = 10^{-2}\,s^{-l}$. (Note that many of these terrain with either an anticyclonic large scale flow or an advancing features can not be considered as 'isolated'.)

In the subsequent sections we shall consider some of the observed flow responses to elongated ridges and isolated features with the scales:

- small amplitude, meso-β/γ scale hills (e.g. Albis - Reuss, rolling hills)
- larger amplitude, meso-α/β scale terrain (e.g. Alps)

These descriptive sections are followed by some theoretical considerations of the flow response.

3.2 Some Observational Features of Orographic Flows

3.2.1 Small amplitude, meso-β/γ scale hills

a) Elongated ridges with flow at normal incidence:

The spectacular display of a train of delicate lenticular clouds located leeward of a mountain ridge is an orographically induced phenomenon that is readily noticed by a ground based observer (see Fig. 3.2 and 3.5). The formation of a family of quasi-stationary lee wave clouds, or the banded clearing of a stratified cloud layer, is visual evidence of a series of oscillatory disturbances set up over and to the lee of the mountain. The clouds form as moist air is lifted by the wave disturbance above its lifting condensation level by the wave disturbance. In essence the air flows through the region of cloud with the adiabatic cooling due to ascent causing condensation on the upstream side, whilst evaporation takes place in the descending air at the downstream

(a) (b)

Figure 3.2: Examples of bands of lenticular clouds that have formed in standing waves to the lee of a mountain range (a). Pronounced Altocumulus undulatus over the Vorderen Vogelsbergkreis (b).

Figure 3.3: Cumulus Lenticularis - a remarkable roll cloud over the Sierras Formed by the Sierra Wave north of Independence, California. Strong updrafts associated with this cloud type. Photography: Bob Bishop,1952.

Figure 3.4: A foehn wall along the Lofoten coast (Norway). Note that the cloud is extending almost down to the sea surface and the presence of an hydraulic jump.

(a) (b)

Figure 3.5: Two further examples of Altocumuli Undulatus. (a) © by Carol Lakomiak, 2003

cloud boundary. The frequent distinctive iridescence of lenticular clouds in early morning or late evening (i.e. at low sun-angles) is a corona effect attributable to the comparatively uniform sized cloud droplets formed in the comparatively laminar airflow (see Fig. 3.6). Lee clouds may occur simultaneously at different height levels if the incident airstream has several, vertically separated, moist layers. At low levels the cloud type is often more ragged due to turbulence, while at high levels the clouds may be composed of ice crystals which often stream downwind in the airflow. In such a situation, with a multi-deck system of mountain waves in the vertical a suitably placed observer may be able to detect a pronounced upstream tilt with height of the wave crest of the system.

(a) (b) (c)

Figure 3.6: Three further illustrations of lenticularis clouds. (a) Pheriche, Khumbu Valley, Nepal, (b) Manganu, Corsica, France, and (c) Mt Rainer, Rockies.

A general climatology of lee waves with respect to synoptic situations and geographical location has been inferred in recent years using high resolution satellite imagery and strategically located radiosonde stations. These studies have demonstrated the ubiquity of this phenomenon with lee waves occuring on average about one day in three in hilly country at temperate latitudes. The main climatological characteristics of lee waves are summarised below:

Vertical Stratification: A lower layer of weak, or quasi-neutral, stability extending from the ground to a height of 1000-2000 m (and occasionally to 4000 m), capped by an intermediate very stable layer (thickness 500-4000 m), with a further layer of weak stability above.

Synoptic Situation: This distinctive vertical structure often occurs in conjunction with either an anticyclonic large scale flow or an advancing warm front.

Vertical wind profile: Wind speed usually increases with height, but not necessarily uniformly or consistently. Similar lee wave systems form at approximately the same location at different periods despite substantial variations in the profile.

and Band Orientation: Bands form parallel to the orography and at some distinctive level that is related to the orographic height. Also a threshold value of the wind speed at this level must be attained for band formation.

Lee waves exhibit a range of forms and occur at various scales. Listed below is a general summary of their typical characteristics:

i) Vertical location: Mostly in the middle or lower troposphere with lenticular altocumuli in the middle levels, $\sim 6000 - 7000$ m and stratocumuli usually in the $1000 - 1500$ m height range. Maximum amplitude of streamlines observed frequently at the height of the stable layer.

ii) Horizontal wavelength: $8 - 30$ km. Observed linear correlation (~ 0.72) between wavelength and mean tropospheric wind speed.

iii) Horizontal extent: From $10 - 300$ km downwind. Inverse relationship between thickness of the very stable layer and the horizontal extent.

iv) Vertical extent: Evidence of wave-activity at great heights above mesa-β scale topography even for comparatively small amplitude terrain.

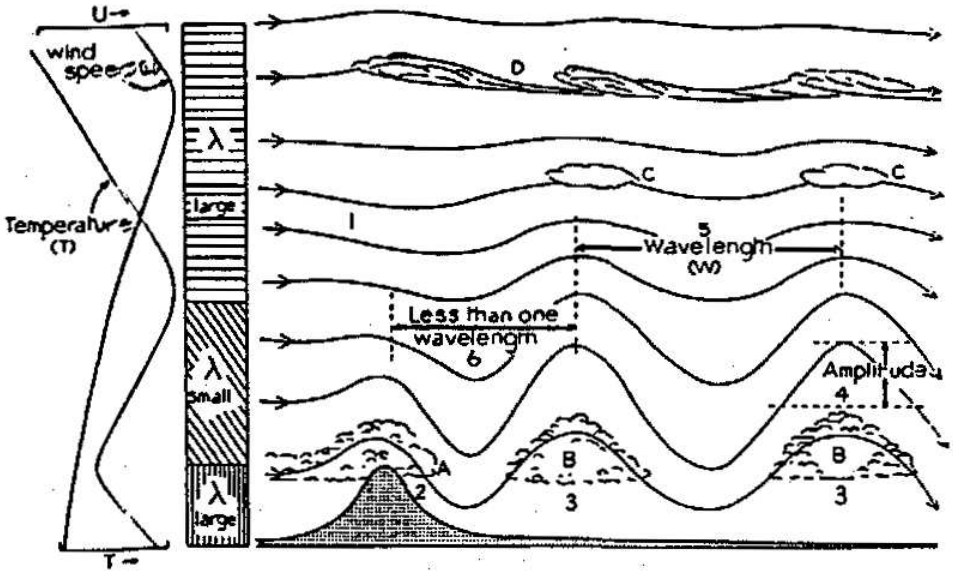

Figure 3.7: Features of air flow across a long mountain range: 1. Downdraught may occur at some levels to windward of ridge. 2. Strong surface wind down the lee slope. 3. Variable surface wind. 4. Maximum amplitude in stable layer. 5. Order of wavelengths: 2-20 miles. 6. First wave crest usually less than one wavelength downstream of ridge. A. Föhnwall. B. Roll cloud. C. Altocumulus lenticularis. D. Cirrus. λ denotes the 'natural wavelength' determined by the airstream wind and temperature conditions and in wave-flow parlance the structure illustrated is described as a 'three layer' troposphere.

Characteristics of low-level response:

In addition to the situation where the airflow speeds-up over the terrain achieving a maximum at the crest, airstreams also often exhibit an asymmetry relative to crest with weak winds upstream and a strengthening of the downslope winds. At larger values of $\mathscr{F}$ (or in the presence of a well-mixed boundary layer capped by an inversion). The upstream flow is sometimes severely retarded or even blocked (Figure 3.8a).

Likewise in a configuration composed of a succession of parallel hills there exist situations for which the air at the level of the crest does not penetrate into the valleys (Figure 3.8b).

b) Isolated Hills:

A variety of complex cloud patterns have been observed on satellite cloud photographs to occur in the neighbourhood of and to the lee of isolated mountains. One distinctive pattern that is often observed in the lee of certain islands (e.g. Ian Meyen, Madeira) is reminiscent of the surface wave pattern behind a ship moving into calm water (- or the related situation of the flow behind a submerged obstacle in a shallow stream). For this situation the cloud pattern is confined to a wedge shaped region with the mountain located at the apex (see Fig. 3.27). There are two types of wave-systems (transverse and diverging waves) that occur either separately or

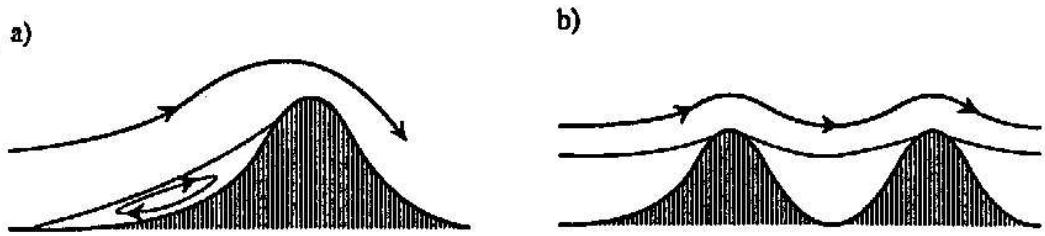

Figure 3.8: Blocked situation in an airflow over an infinitely wide mountain ridge (a) and over a succession of parallel mountain ridges (b).

simultaneously within the wedge region.

These waves are observed when the prevailing vertical stratification is similar to that noted earlier for two-dimensional trapped lee waves viz. a strongly stable layer (often an inversion) from approximately 500 to 3000 m in with a nearly neutrally stable layer below and weakly stable layer above.

The transverse waves are aligned perpendicular to the flow and are more evident in comparatively light wind situations. They are the counterpart for this mountain configuration of the trapped lee waves discussed earlier.

The other waves type - the diverging wave - are aligned so that their crests meet the incident flow at an acute angle. The envelope of these crests demarks the outer boundary of the wedge and can stretch for several hundred kilometers (see Fig.3.27).

In the isolated hill case weak low level stratification with a capping inversion and high terrain is strong quasi-two dimensional flow around the terrain at low-levels and the occurrence of complex flow-phenomena, including the possibility of a train of vortices, in the lee.

3.2.2 Major meso-α/β scale mountains

Orographic features of larger (meso-α/β) horizontal dimensions tend to also be associated with substantially higher elevations. Here we consider such terrain features and devote particular attention to the nature of the flow response in the neighbourhood of the European Alps.

The main ridge of this mountain chain is aligned approximately WSW-ENE at about 46.5° N. Climatologically the chain is situated downstream of the split in the North-Atlantic jet, and the prevailing flow at 850 hPa is a comparatively weak WNW airstream. The ridge itself is characterised by a length, width and height of respectively 1000, 200 and 2.5 km. These vertical and horizontal scales betoken a potential for a significant finite amplitude flow response ($\mathscr{F} \geq 1$) and appreciable ageostrophic effects ($Ro \geq 1$).

One pointer to such effects is the frequent depiction on surface charts of cross-Alpine pressure gradients that are far in excess of those that prevail over most of the remainder of Europe. In the near Alpine region these enhanced gradients are usually accompanied by an 'S' shaped isobaric distribution aligned across the Alps (See fig.3.93.9b). This pattern is commensurate with elongated meso-scale high and low pressure pillows located respectively on the windward and lee slopes. The associated synoptic scale surface pressure field often signifies a split of the

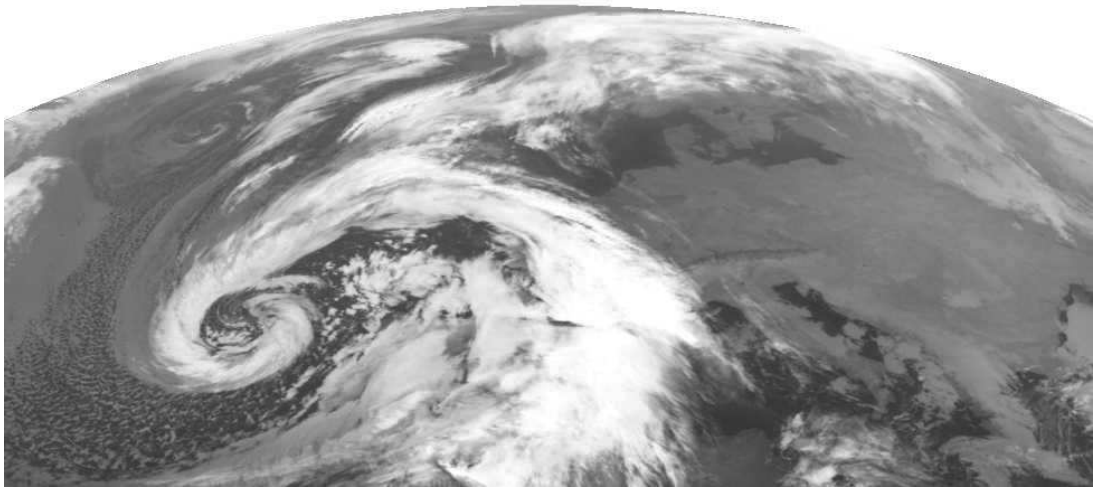

(a)

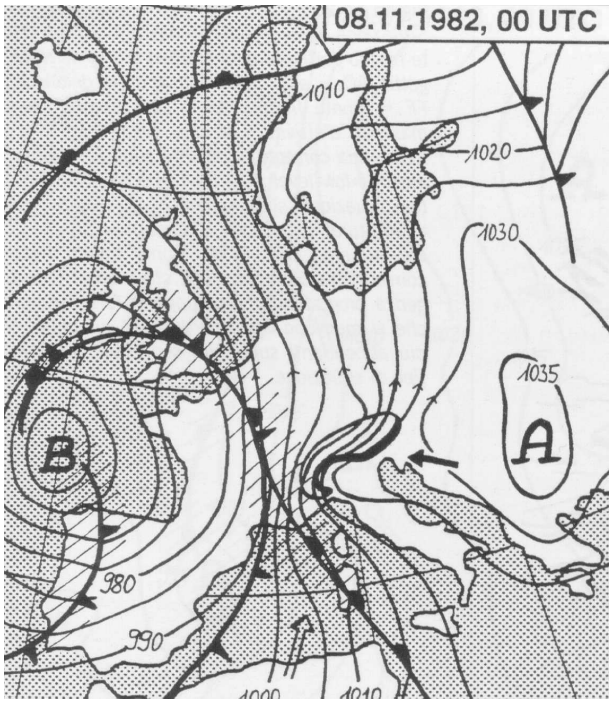

(b)

Figure 3.9: Infrared image of a spectacular 'south foehn'-situation as taken by Meteosat-2 on November 7, 1982 at 6 UTC (a) and the corresponding synoptic surface chart (b). The observed pressure gradient across the Alps reached a record of 20 hPa causing winds of up to 190 km/h across the Gottard Pass. While Locarno observed an air temperature of 1°C with mixed rain and snow, skies above Zürich were clear with a temperature of 25°C. (source: EUMETSAT.)

geostrophic flow around the Alps. This indicator of splitting is further emphasized by inspection of the wind roses compiled for near Alpine radiosonde stations. These indicate, in contrast to mountain removed stations, a predilection for an along-ridge flow at levels beneath the crest of

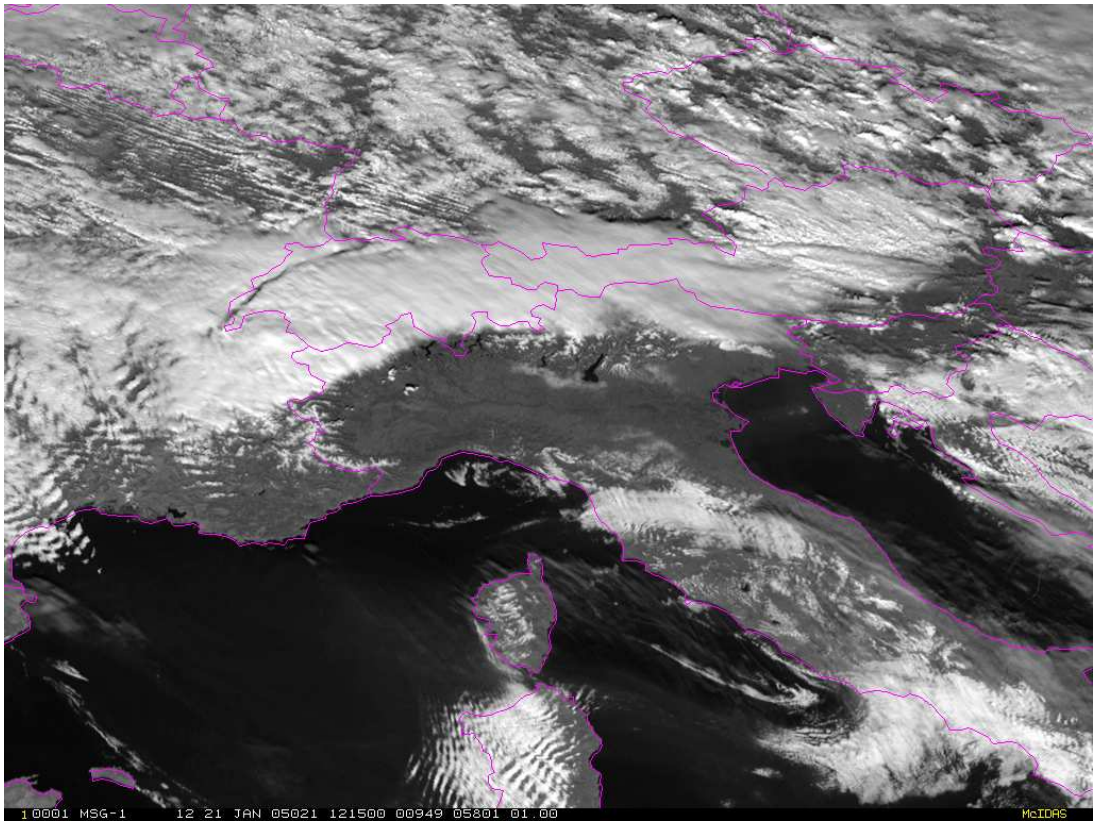

Figure 3.10: HRV image of a spectacular 'north foehn'-situation as taken by Meteosat-8 on January 21, 2005. Note the stau cloudiness over the Alps extending some 50 km downwind of the main mountain range (Locarno is overcast with weak precipitation, Lugano is clear). At Stabio (TI), the arrival of the foehn wind rose the surface temperature from -2.6°C to above +13°C within 24 h. Note the band-clouds in the lee of meso-β/γ-scale hills as the Massif du Midi and the narrow gap in the clouds along the southern side of the Jura mountains. This gap is produced by the 'Joran' or 'Jorat' wind, a mini-foehn effect. (source: EUMETSAT.)

the Alpine chain.

In the following sub-sections we examine briefly the nature of the response for the disparate situations when the air upstream is quasi-steady and directed normal to, and tangential to, the main ridge.

a) Normal incidence:

The atmosphere above the Alpine foreland during periods of flow from the NW-NE quadrant indicates that the upstream low-level airflow is characterized by

- the forementioned high pressure pillow on the immediate north side,
- substantial channeling/blocking of the airflow within an extensive domain of width $\sim 100 - 200$ km, and a height comparable to the mean crest height of the Alpine ridge,
- a stable layer capping this modified region.

A striking feature of the flow over the foreland during southerly flow periods (i.e. when it corresponds to the lee side) is the Foehn with its strong, anomalously warm downslopewind

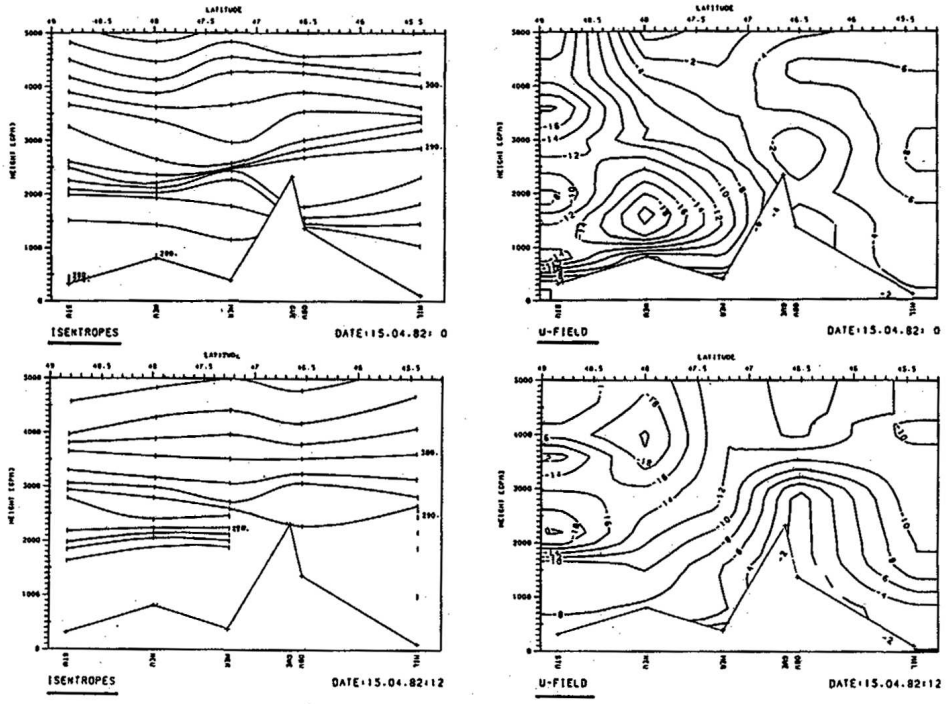

Figure 3.11: Alpine cross section at 00 Z and 12 Z on 14 April 1982 of the potential temperature (left) and the along-ridge wind component.

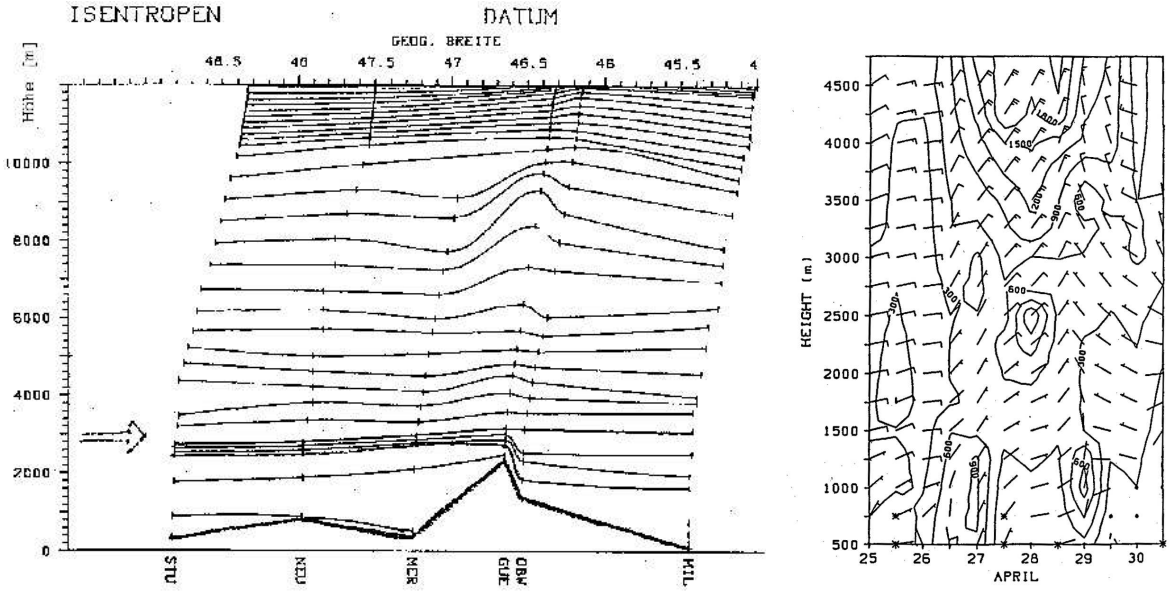

(a) (b)

Figure 3.12: Cross-section along the alps during a period of northerly flow (a). Time-height section of the airflow and the accompanying values of $h^* = U/N$ (b).

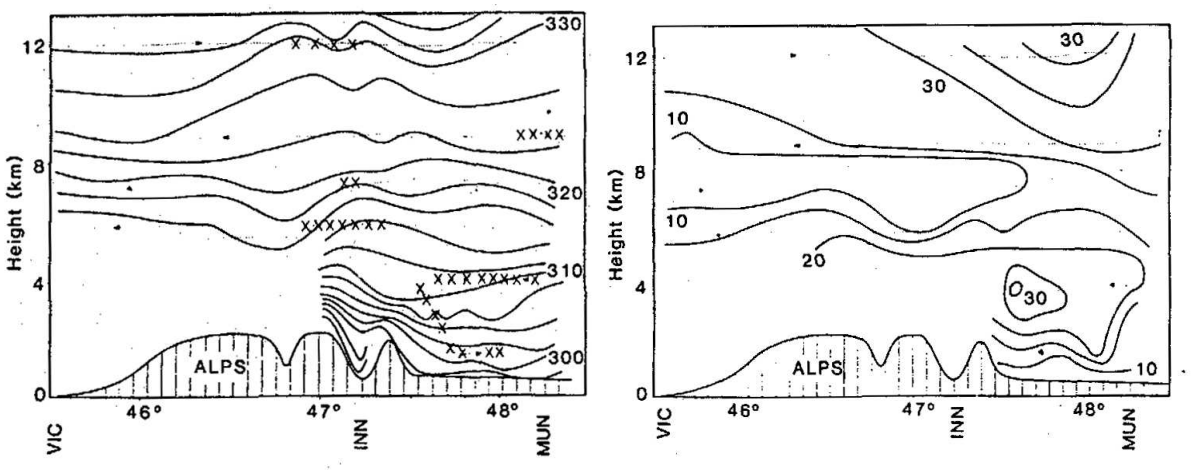

(a) (b)

Figure 3.13: Cross section along the alps during a period of northerly flow (a). Time-height section of the airflow and the accompanying values of $h^* = U/N$ (b).

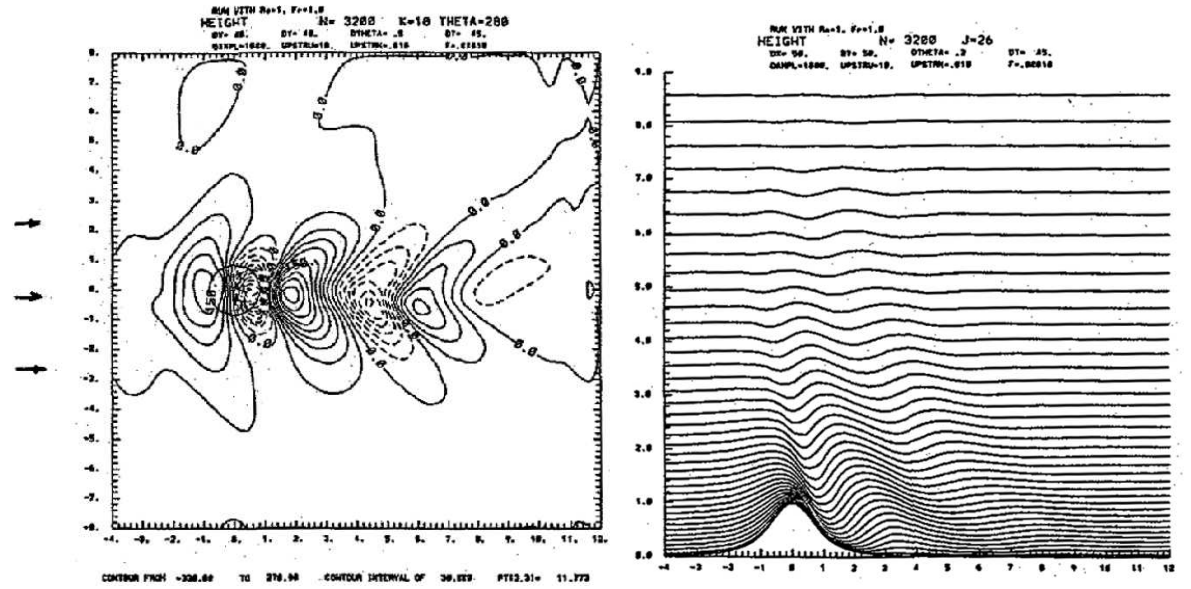

(a) (b)

Figure 3.14: Non-linear numerical simulation for $Ro = 1$ and $\mathscr{F} = 1$.

regime (see Fig. 3.16). Illustrations are provided of the atmospheric vertical structure that prevailsin a section across the mountain during such episodes for both the Chinook in the Rockies (see Fig.3.2.2) as well as South respectively north Foehn in the Alpine region (see Fig.3.9 and 3.11 respectively Fig.3.10). In the former case features of interest are evidence of

- trapped lee waves and an almost-stagnant region downstream,
- longer wavelength features at higher elevations,

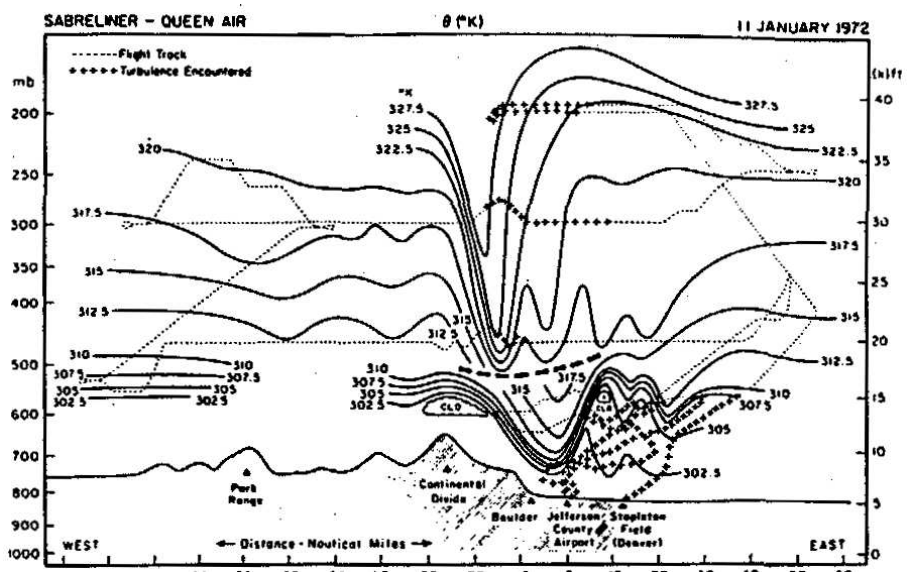

(a)

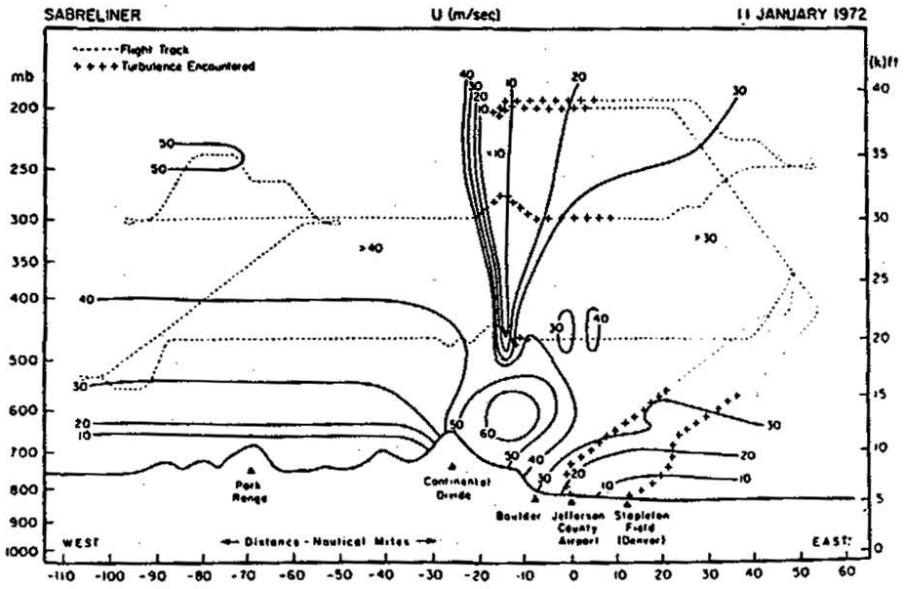

(b)

Figure 3.15: (a) Cross section of potential temperature field in K over the mountains and foothills as obtained from analysis of the Queen Air and Sabreliner data on 11 January 1972. Data above 500 mb are exclusively Sabreliner taken from 1700-2000. data below 500 mb are primarily Quen Air taken from 1330-1500 MST. Flighttracks are indicated by the dashed lines, except by crosses in turbulent portions. At this time it is not possible to determine whether the apparent westward displacement with height of the major features is real or related to the time difference between the two flights. Windstorm conditions on the ground extend eastward to the location where the isentropes rise sharply, a few miles east of the origin at the Jefferson County Airport. (b) Westerly wind component cross section for 11 January 1972.

- large amplitude features above the terrain (parcel excursion some kilometers) accompanied by an upstream slope of the phase lines, possible wave-overturning and localised turbulence.

For the Foehn case the descent of the isentropic surfaces to the lee is again evident whereas the wave activity is somewhat less apparent. To the north there is usually a cold surface layer and the Foehn air ascends over and denudes this layer. Surface pressure charts display the forementioned characteristic Foehn trough to the lee.

a) Tangential incidence:

A frequent and climatologically significant feature of the atmosphere during periods when the geostrophic flow is aligned nearly along the contours of a ridge is the occurrence of a low-level jet. Regions of occurrence include in addition to the northern slopes of the Alps, the eastern slopes of the Rockies, the Andes and the East-African highlands (See Fig3.16).

The jet is usually located within or at the top of a substantially mixed planetary boundary layer (P.B.L). When the jet is land-based it usually exhibits a strong diurnal modulation in concert with the diurnal changes of the P.B.L. In the Alpine region the jet is closely linked with the so-called Bise wind.

3.3 Some Theoretical Considerations

Physical insight on the nature of the flow response to orography can be explored utilizing theoretical concepts and undertaking numerical simulation or laboratory analogue experiments. However the sheer variety of orographic profiles (- and concomitant variation in the relevant dimensionless parameters) effectively limits studies to key prototype situations or to some particular terrain feature that is of special interest.

Here we consider two such prototype configurations: -A 'Witch of Agnesi' infinite ridge and a bell-shaped circularly symmetric obstacle. In both cases the orography is assumed immersed in an incompressible atmosphere that is unbounded above and the incident airstream is taken to be of uniform flow and stratification (i.e. U and N constant). The nature of the response is then sought in the parameter space of (Ro,$\mathscr{F}$). Note that the $\mathscr{F} \to 0$ end of this 'lagoon' is the linear theory limit of small topographic perturbations (c.f. $0\eta \to 0$), and that the lateral shores correspond to the strongly quasi-geostrophic ($R \ll 1$) and the non-rotating ($Ro \to \infty$) limits. In the following sub-sections an overview is provided of the known features of the response.

3.3.1 Case I: The infinite Ridge

a) Low Topography ($\mathscr{F} \to 0$ limit)

The linear wave theory developed earlier. should provide some information relevant to small amplitude orography and act as a guide and a starting point for the study of other flow configurations.

It was shown earlier, that the dispersion relationship takes the form

$$\omega = Uk \pm \left[\frac{N^2K^2 + n^2f^2}{\delta K^2 + n^2}\right]^{1/2} \qquad \text{with } K^2 = (k^2 + l^2) \tag{3.1}$$

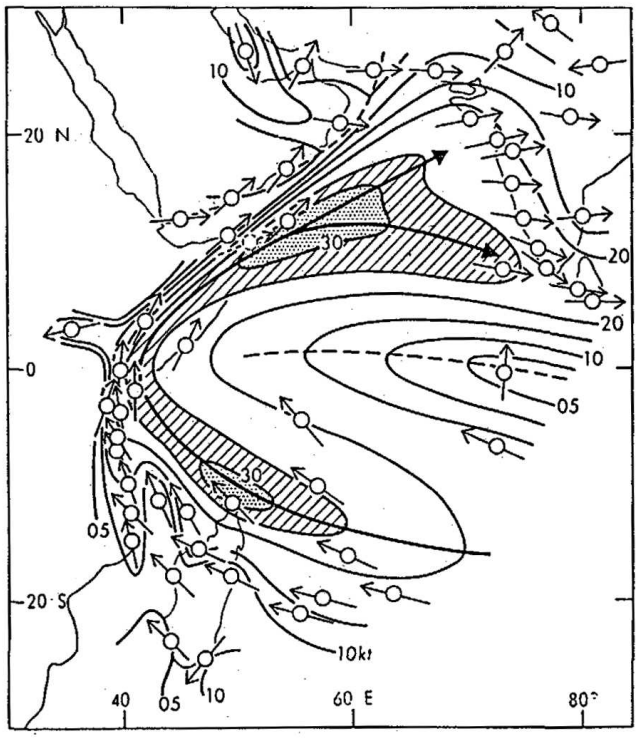

(a)

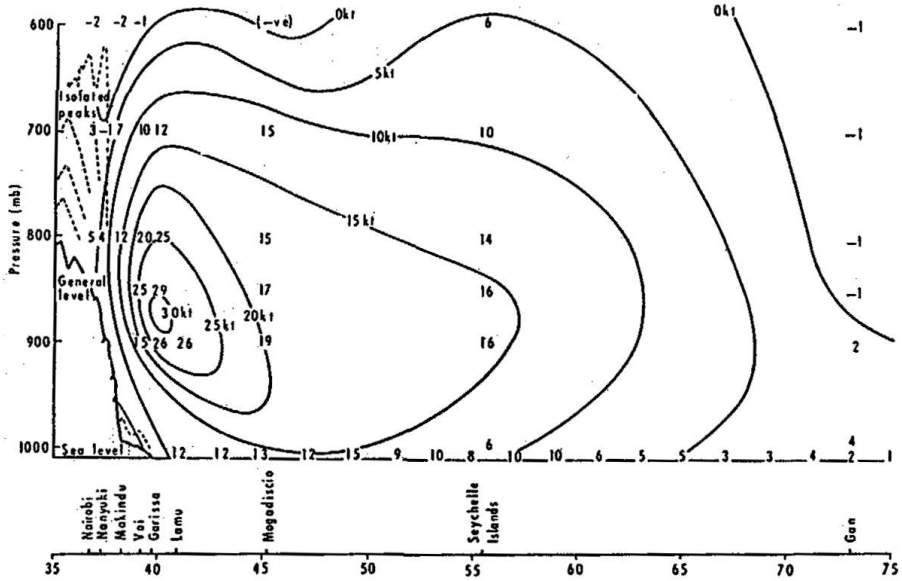

(b)

Figure 3.16: (a) Monthly mean airflow at 3000 ft (1 km) in July. Bold arrows: Major streamline, axis of maximum flow. Solid lines: Isotachs, at 5 kt intervals and dashed lines: Axis of maximum wind. (b) Cross section of mean meridional flow at the Equator in July.

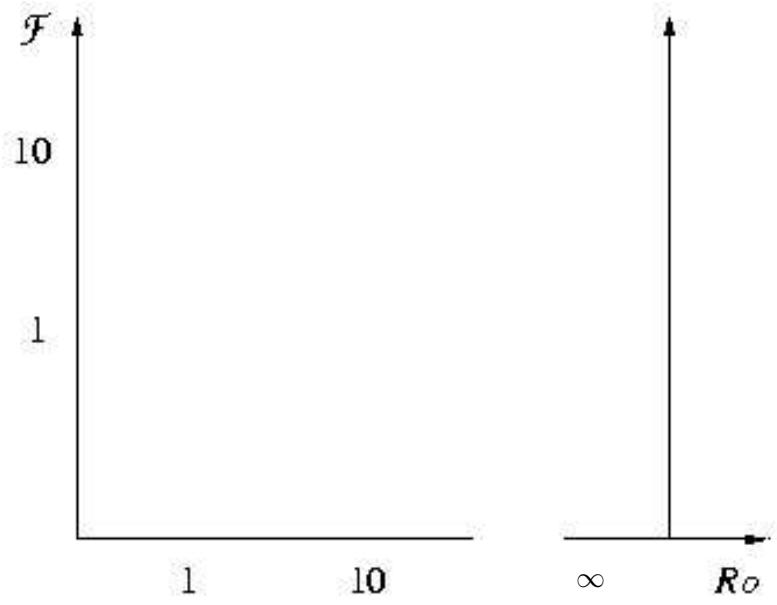

Figure 3.17: Flow response to prototype problem: Ridge orography; Incompressible, inviscid fluid on an f-plane; Witch of Agnesi Terrain; Uniformly structured incident flow (N and U constant); Appropriate parameterspace: Ro and $\mathscr{F}$.

It follows that for a steady response

$$Uk = \pm \left[\frac{N^2K^2 + n^2f^2}{\delta K^2 + n^2} \right]^{1/2} \tag{3.2}$$

and hence

$$n^2 = K^2 \left[\frac{N^2 - \delta U^2 k^2}{U^2k^2 - f^2} \right] \tag{3.3}$$

For $N > f$, vertical propagation is confined to the band $(N/U) > k > (f/U)$, i.e. $(2\pi U/N) < \mathscr{L} < (2\pi U/f)$

Furthermore for the steady state flow response the components of the group velocity are given by,

$$w_g = \frac{\partial \omega}{\partial n} = Ukn \cdot \frac{1 - \frac{f^2}{U^2k^2}}{\delta K^2 - f^2}, \tag{3.4}$$

$$u_g = \frac{\partial \omega}{\partial k} = U[1 - \Delta], \tag{3.5}$$

$$v_g = \frac{\partial \omega}{\partial l} = U\frac{1}{k}\Delta, \tag{3.6}$$

where

$$\Delta = \frac{\left\{ \left(\frac{N}{U}\right)^2 - \delta k^2 \right\}}{\delta K^2 + n^2}, \text{ and } (\delta K^2 + n^2) = K^2 \cdot \frac{N^2 - \delta f^2}{U^2k^2 - f^2} \tag{3.7}$$

The perturbing effect of the mountain upon an incident airstream can be interpreted as a source for wave energy. Hence, for a terrain feature located near $(x, y, z) = (0, 0, 0)$, then outward radiation of wave energy implies $w_G > 0$ for $z > 0$, and $v_G > 0$ (< 0) for $y > 0$ (< 0).

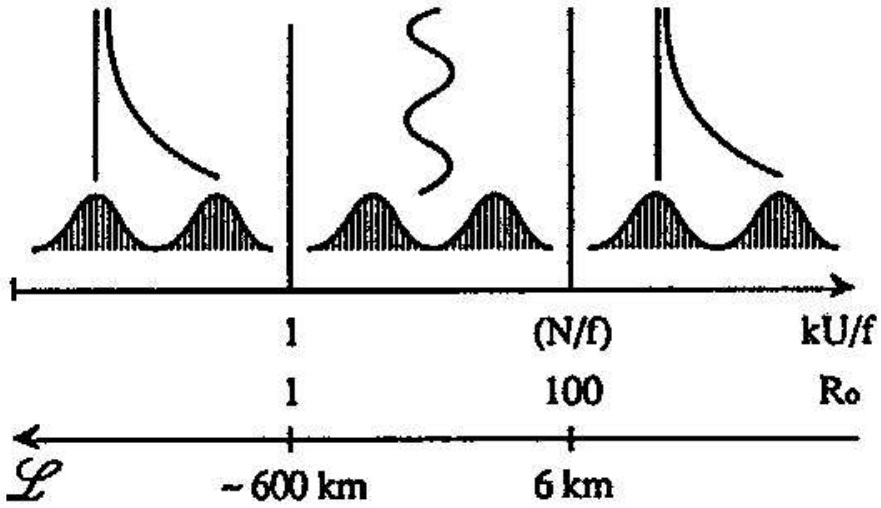

Figure 3.18: Vertical propagation mode as a function of horizontal wavenumber.

It follows that $(kn) > 0$ for a wave mode in the band $[f/U, N/U]$. Now the lines of constant phase in an (x, z) plane is given by

$$z = -\left(\frac{k}{n}\right) x + \left(\frac{\Phi c}{n}\right) \tag{3.8}$$

Thus in association with vertical energy propagation {with $(k, n) > 0$} the lines of constant phase will slope upstream with height. (This result implies an asymmetry of flow up and downstream of the mountain peak, and hence there is the possibility of a wave-drag effect on the mountain. These inferences are illustrated in the figure below.

Note from (2.12),

$$\frac{\partial}{\partial x}\left[Uu' + \frac{p'}{\rho_0}\right] = fv' \tag{3.9}$$

and thus if

$$\frac{\left\|\frac{Uu'}{L}\right\|}{\|fv'\|} \gg 1, \tag{3.10}$$

then

$$u' \approx (-p') \tag{3.11}$$

i.e. flow retardation accompanied by high pressure.

The direction of energy propagation (i.e. the ray path) in the (x, y) plane is given by

$$\tan(\alpha) = \frac{w_G}{u_G} \tag{3.12}$$

where α is the inclination of the ray path to the horizontal. Use of (3.4 to 3.6) and (3.9) indicates the following:

The foregoing inferences regarding the nature of the response have been based purely on group velocity concepts. A formal development of the solution for meso-β/γ scale ($f \equiv 0$) flow of an uniform stream of constant stratification over two-dimensional sinusoidal terrain is given in the Appendix. The two forms of solution for $k > (N/U)$, $k < (N/U)$ are shown in Fig.3.3.1,

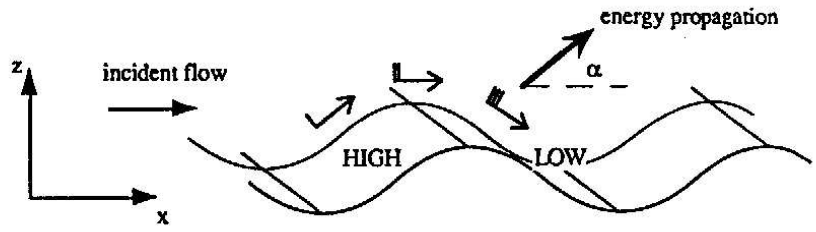

Figure 3.19: Schematic of flow over sinusoidal terrain and vertical energy propagation

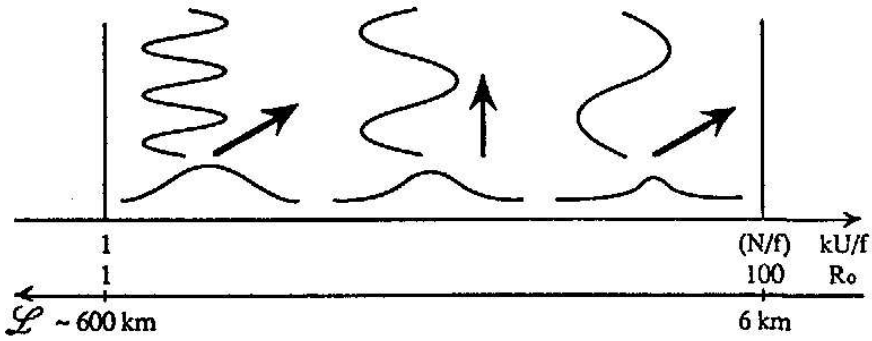

Figure 3.20: Refined vertical energy propagation modes in the range of vertical propagating waves.

and the main characteristics of the solutions are:

For case (a) the phase lines are vertical and the disturbance decay with height.

For case (b) the phase lines tilt backward into the mean wind and propagate energy away from the orography. In this case the flow is asymmetric with low speed and high pressure on the windward side and high speed and low pressure on the leeward side. It follows that there is a pressure drag on the ridges.

Note also that an arbitrary two-dimensional orographic profile can be Fourier decomposed into contributions of the form $\{e^{ikx}\}$. The flow response to such a profile can then be evaluated by treating each 'k' component as in the Appendix and then synthesizing the components. Illustrations of the result of such a procedure are shown in Fig.3.22. Orography characterised by a small half width $L \ll (2\pi U)/N$ produces a predominantly evanescent response, whilst orography with $(2\pi U)/N \ll L \ll (2\pi U)/f$ yields a hydrostatic wave response associated with quasi-vertical energy ray path. In the latter case the flow asymmetry is again evident.

These theoretical examples (see also Fig. 3.23 and 3.24) are illuminating and are consistent with some of the observational features.

b) High Topography of Intermediate Width ($\mathscr{F}$-finite; $Ro \gg 1$ limit)

The intermediate width is taken to refer to scales of $30 - 100$ km so that the wave response is

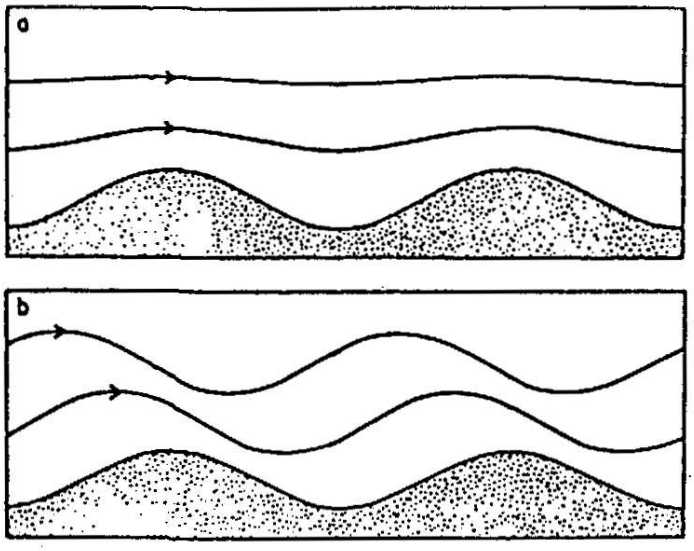

Figure 3.21: The steady inviscid flow over two-dimensional sinusoidal topography. (a) Little or no influence of buoyancy, $Uk > N$. the disturbance decays upward with no phase line tilt. (b) Strong buoyancy effects, $Uk < N$. The disturbance amplitude is constant with height while the lines of constant phase tilt strongly upstream.

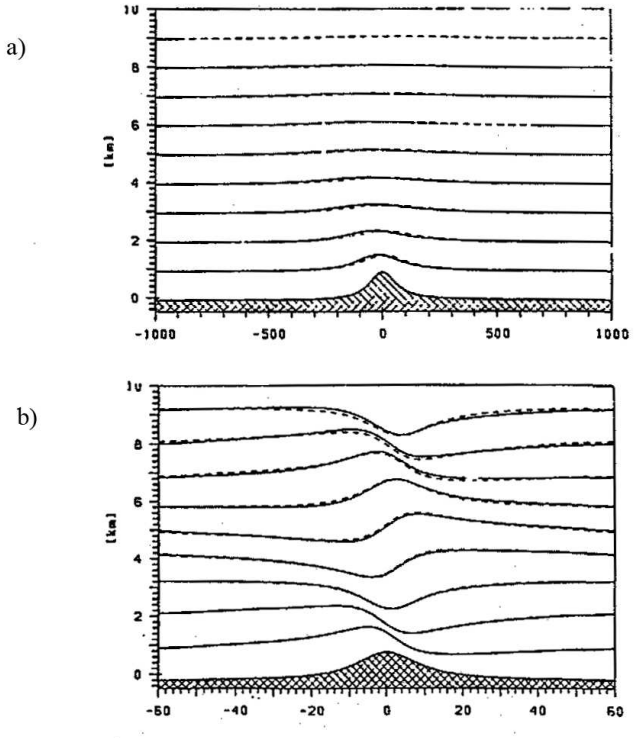

Figure 3.22: Linear theory results for flow over a two-dimensional ridge of an incident airstream of uniform U and N. (a) $Ro \ll 1$. and (b) $Ro \gg 1$

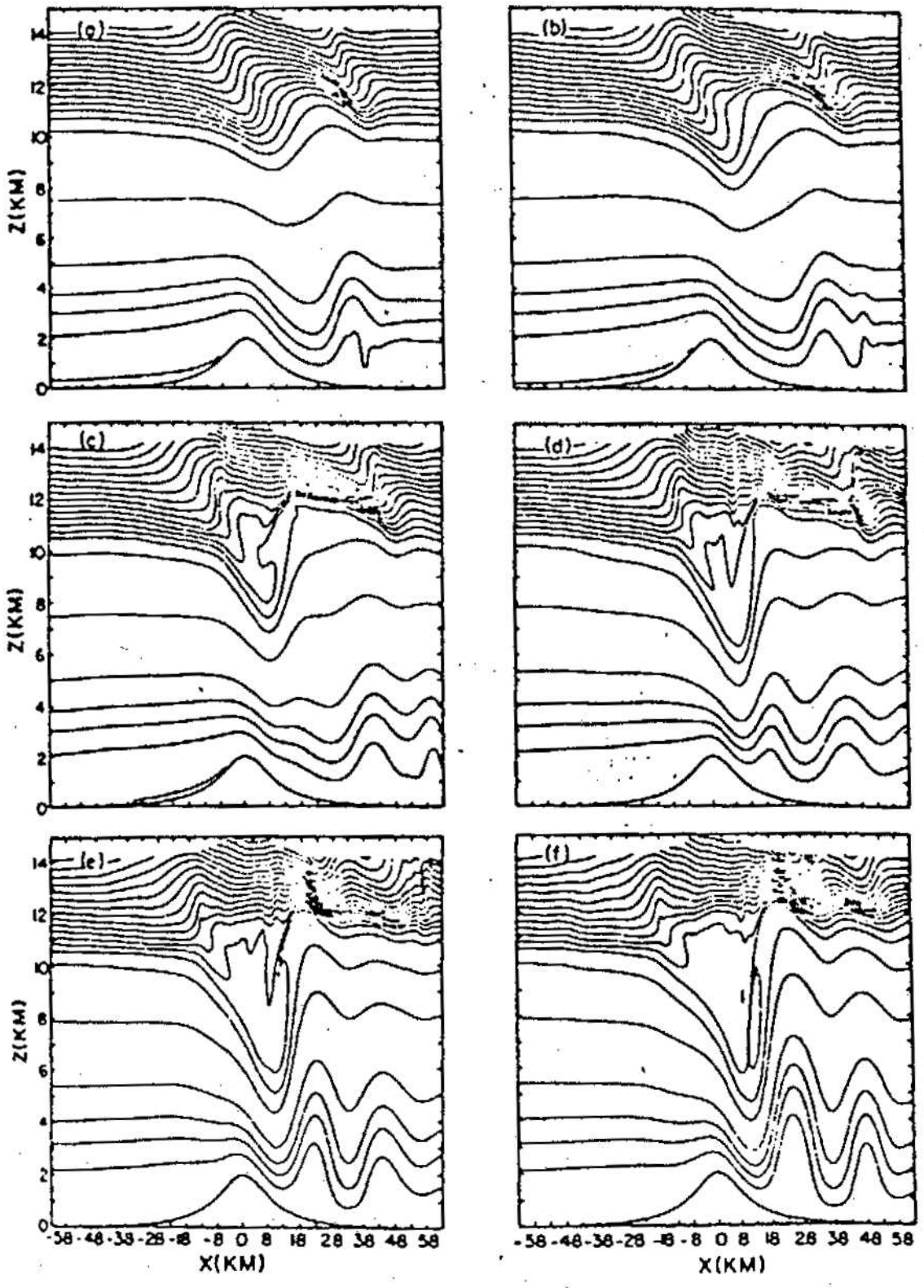

Figure 3.23: Simulation of severe downslope windstorm over Colorado Rockies using non-linear, non-hydrostatic theory (Peltier and Clark, 1979)

essentially hydrostatic in the $\mathscr{F} \to 0$ limit. Now the finite amplitude of the orography induces

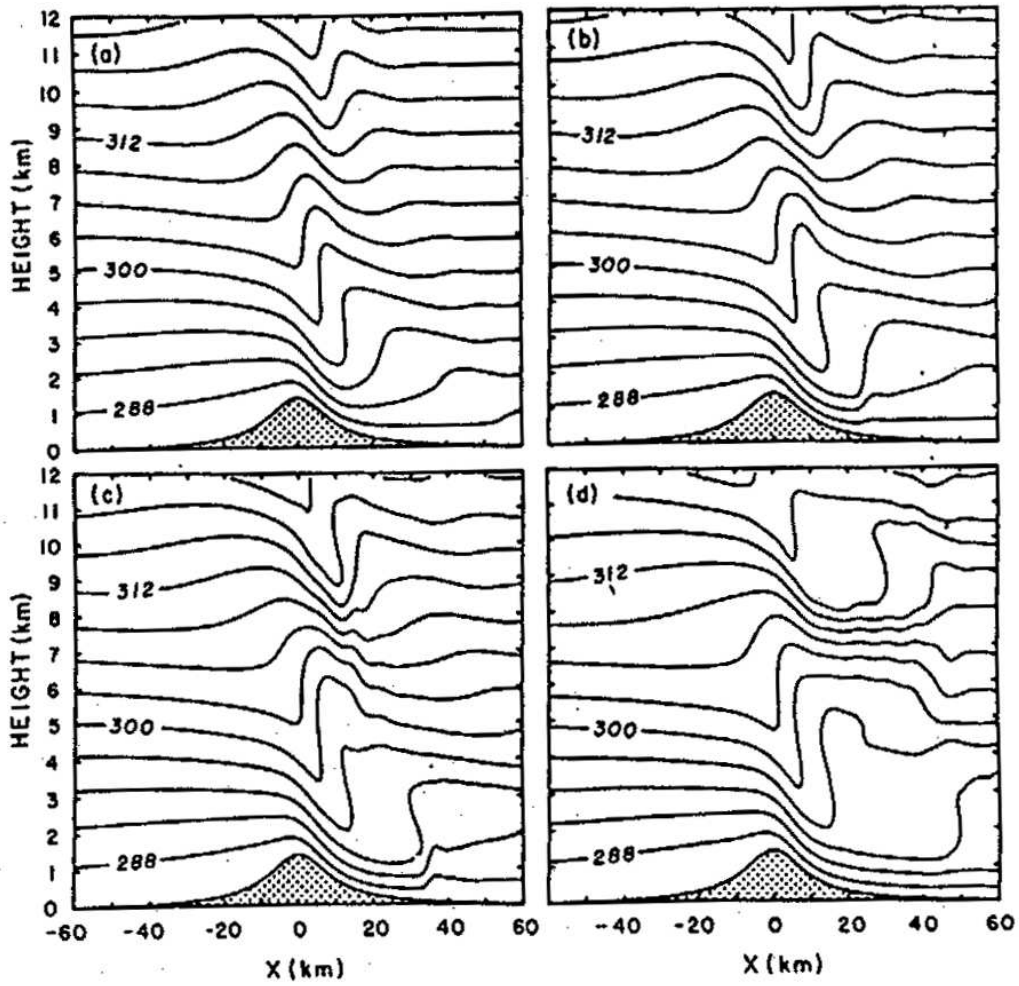

Figure 3.24: ?Same as figure 3.23 but for changed boundary conditions?

a non-linear flow response. Theoretical studies and numerical model simulations reveal several 'transition' features:

- as $\mathscr{F}$ increases the wave amplitude and vertical flux of momentum increases until the wave attains an overturning amplitude at an elevated location for $\mathscr{F} \sim 0.8$. In the more general case the value of $\mathscr{F}$ required for overturning is a function of the ridge shape and the upstream profile. At and beyond the overturning amplitude the flow develops a quiet zone between the overturning level and a surface layer of considerably enhanced downslope and lee-side winds with an accompanying large increase in the pressure-drag. These features have some of the characteristics of a hydraulic jump phenomenon.

- with a further increase of $\mathscr{F} \sim 1.0 - 1.3$ the flow upstream of the crest is retarded to the point where flow reversal and upstream blocking occurs. This layer has a depth $\sim (\eta - U/N)$ and extends far-upstream. Some insight on these results can be gained from noting that:

  i) The parameter $\mathscr{F}$, viewed as a measure of the ratio of the energy required to lift a parcel through a height h in an uniformly stratified environment to the kinetic energy of the incident flow, implies that a crude estimate of the depth (H_B) of blocked flow is $H_B \sim (\eta - U/N)$.

ii) For two dimensional, hydrostatic, non-rotating flow the dispersion relationship of linear wave theory is given by $\omega = Uk \pm N \cdot k/n$
and $\omega = 0$

for either	$U = N/n$	$\Rightarrow$	$u_G = U - N/n$
or	$k = 0$	$\Rightarrow$	$v_G = U \pm N/n$
			$w_G = 0$

The second situation implies a modification of the mean flow by horizontal columnar energy propagation. This modification is both up and downstream if $(N/\eta) > U$ and it is probable that the vertical wave number n would scale with the terrain height (say $n \sim \pi/4h$) and thus an upstream effect might be anticipated for $\mathscr{F} \geq 4/3$.

iii) Hydraulic theory of shallow water flow (see later) appears to offer an useful conceptual framework for some aspects of the flow response (c.f. the upstream propagation 'bore', the retreating lee-side hydraulic jump).

c) High Topography of Larger Width ($\mathscr{F}$-finite; $Ro \ll 1$ limit)

The linear wave theory for the $Ro \ll 1$ domain is essentially quasi-geostrophic. An indication of the response for finite $\mathscr{F}$ values can be obtained by considering semi-geostrophic flow (i.e. geostrophy of only the along-ridge flow component) over isentropic terrain. The amplitude of the evanescent response can be shown to be proportional to $(1 - Ro \cdot \mathscr{F})^{-1}$ with the isentropes fusing onto the crest as $Ro \cdot \mathscr{F} \rightarrow 1$. Again for more general configurations the critical $Ro \cdot \mathscr{F}$ value is dependent upon the shape of the orography.

d) The 'inner-Lagoon' ($\mathscr{F} \geq 1; Ro \sim 0.5 - 5$)

Simulations undertaken in this domain indicate that the low-level blocked region extends upstream only a finite width - order of a Rossby radius of deformation based upon the crest height (Nh/f) The almost stagnant region is surmounted by a pseudo-semi-geostrophic regime with air accelerating to the crest and a strongly ageostrophic lee side regime with large amplitude or breaking waves.

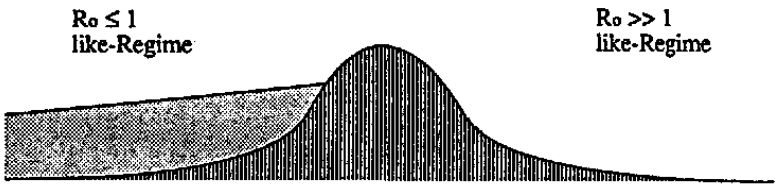

Figure 3.25: Schematic of 'inner lagoon'

3.3.2 Case II: Circular Orography

a) Low Topography ($\mathscr{F} \rightarrow 0$)

Some understanding of the wave response in the wake of an isolated hill also be obtained with linear theory. It was noted earlier that two forms of waves are frequently observed - transverse

and diverging waves. The former can be viewed as the counterpart for this flow configuration of the trapped lee waves discussed earlier.

An understanding of the divergent wave type is sought in terms of phase and group velocity considerations of hydrostatic three dimensional gravity waves (- the counterpart of the purely vertical propagating modes in the ridge situation). For these waves the appropriate dispersion relationship is (2.15b) with $(k^2 + l^2) \ll n^2$

$$\hat{\omega}^2 = N^2 \frac{k^2 + l^2}{n^2} \tag{3.13}$$

with the phase given by

$$\Phi = kx + ly + nz - \omega t. \tag{3.14}$$

It follows that the frequency is given by the equation

$$\omega = Uk \pm N \frac{1}{n}(k^2 + l^2)^{1/2} \tag{3.15}$$

and stationary waves ($U_p \equiv 0$) must satisfy the relation

$$U = N \frac{(k^2 + l^2)^{1/2}}{nk} \tag{3.16}$$

The component group velocities are given by

$$u_G = U - \frac{N}{(k^2+l^2)^{1/2}}(k/n) = U \frac{l^2}{k^2 + l^2} \tag{3.17}$$

$$v_G = U - \frac{N}{(k^2+l^2)^{1/2}}(l/n) = -U \frac{l \cdot k}{k^2 + l^2} \tag{3.18}$$

$$w_G = U - \frac{N(k^2+l^2)^{1/2}}{(n^2)} = \frac{U^2 k^2}{N \cdot (k^2 + l^2)^{1/2}} \tag{3.19}$$

Thus we have downstream and upward vertical energy propagation, associated with positive (negative) values of v_G for wavenumber (l) assuming negative (positive) values. From (3.14) we conclude that in the horizontal and vertical the phase lines will radiate outward and downstream from the source.

The ray paths for the energy can be derived from (3.10) and the coordinates (x^*, y^*, z^*) of the paths will be given by,

$$\frac{z^*}{x^*} = \frac{w_G}{u_G} = \frac{U}{N}\left(\frac{k}{l}\right)^2 (k^2 + l^2)^{1/2} \tag{3.20}$$

$$\frac{y^*}{x^*} = \frac{v_G}{u_G} = -\frac{k}{l} \tag{3.21}$$

$$\frac{z^*}{y^*} = \frac{w_G}{v_G} = -\frac{U}{N}\left(\frac{k}{l}\right)(k^2 + l^2)^{1/2} \tag{3.22}$$

Equations (3.20-3.22) can be combined to show that the wave energy will be concentrated near the parabola defined by

$$y^{*2} = \frac{U}{N} \frac{1}{(k^2 + l^2)^{1/2}} z^* x^* \tag{3.23}$$

The dominant wave mode for a symmetric mound will be such that

$$(k^2 + l^2)^{1/2} \approx \frac{1}{a} \tag{3.24}$$

where a is the scale width. In this case

$$y^{*2} = \frac{N}{U}(a)z^*x^* \tag{3.25}$$

This semi-qualitatively derived formula is in reasonable accord with the observed diverging cloud pattern.

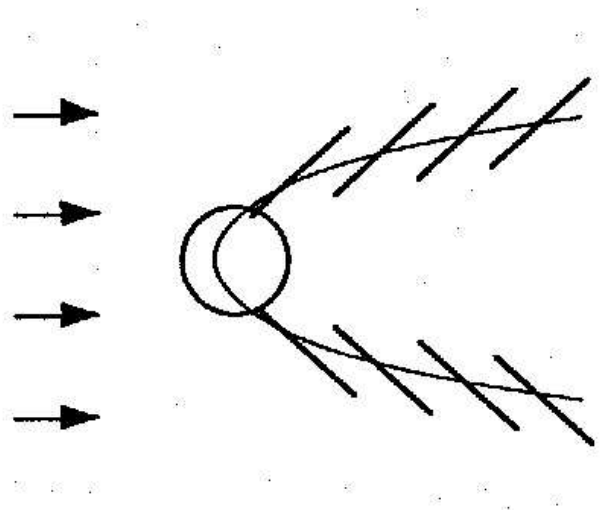

Figure 3.26: Schematic lee-wave train of clouds past a circular mound.

In addition to the foregoing general approach based upon group velocity considerations it is again possible, as for the ridge case, to consider the response of a particular localized obstacle. The procedure now involves the decomposition of the terrain specification into a double Fourier series, solving the three-dimensional wave problem for an arbitrary doubly sinusoidal bottom boundary followed by a Fourier synthesis of the wave solutions to obtain the real-space solution. The resulting patterns confirm the occurrence of the V-shaped wave pattern and show a downslope regime and lee-side convergence for wide range of Ro values. Also a mountain-bound anticyclone induced by vortex compression is evident for the $Ro \geq 1$ region.

b) High Topography of Intermediate Width ($\mathscr{F}$ – finite; $Ro \gg 1$ limit)

Very stable stratification ($\mathscr{F} \gg 1$) acts to suppress vertical displacements of fluid parcels and serves to induce a symmetrical 'almost' horizontal flow around the topography. In such a configuration conventional viscous boundary effects would help induce a separation of the flow in the boundary layer, the formation of a wake and the shedding to the lee of vortices with quasi-vertical axes. For $\mathscr{F} \leq 1$ the limited lateral width inhibits somewhat the amplitude of the hydrostatic buoyancy wave and the occurrence of wave overturning. For $\mathscr{F} \geq 1$ there is some evidence of upstream blocking and of the development of convoluted lee vortices even in the absence of viscous effects.

c) High Topography of Larger Width ($\mathscr{F}$ – finite; $Ro \ll 1$ limit)

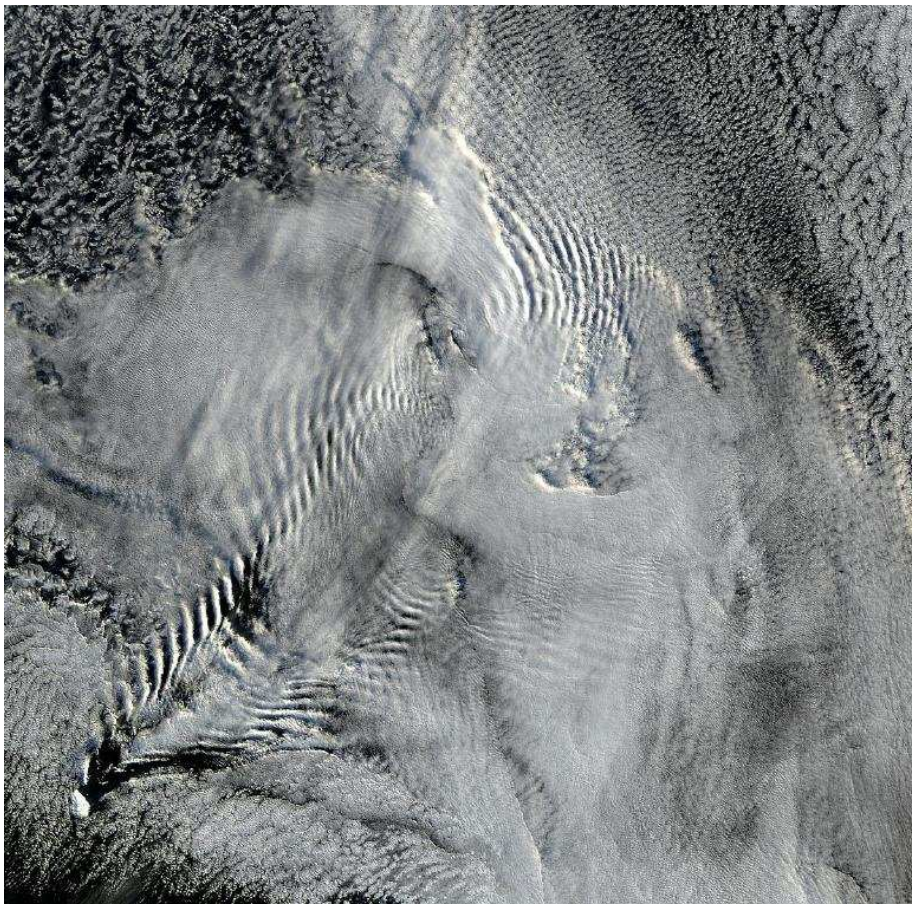

Figure 3.27: Ship-wave-shaped wave clouds induces by Peter I Island, (bottom left corner) off West Antarctica, perspective from Satellite Terra on March 28, 2004.

The geostrophic and semi-geostrophic flow response to isentropic terrain corresponds to a mountain bound anticyclone whose amplitude again increases with $Ro\mathscr{F}$. For $\mathscr{F} > 1$ the strength of this vortex can overcome the strength of the incident flow and a Taylor cap - a conical region of cut-off, closed, streamlines - forms over the elevated terrain. Fusion of the isentropes onto the crest occurs as $Ro\mathscr{F} \to 1/2$.

In the lagoon domain of $Ro\mathscr{F} > 1/2$ with $\mathscr{F} \gg 1$ (and hence $Ro \ll 1$) there is some indication that, as for the $Ro \gg 1$ situation, the flow splits around the terrain. Now however the pattern is asymmetric with strong ascent on the right flank (looking downstream) and the reverse on the left flank.

d) The 'Inner Lagoon'

As in the infinite-ridge case some flow simulations indicate that region exhibits features akin to both the $Ro \ll 1$ and the $Ro \gg 1$ regimes. However there are gaps in our knowledge and understanding of this part of the 'Lagoon'.